Modelling Pinchoff and Reconnection in a Hele-Shaw Cell Part II: Analysis and Simulation in the Nonlinear Regime

Hyeong-Gi Lee and J.S. Lowengrub*

School of Mathematics, University of Minnesota, Minneapolis, MN 55455.

J. Goodman

Courant Institute of Mathematical Sciences, New York University, NYC, NY 10012.

(June 4, 2001)

Abstract

This is the second paper in a two part series in which we analyze two diffuse interface models to study pinchoff and reconnection in binary fluid flow in a Hele-Shaw cell with arbitrary density and viscosity contrast between the components. Diffusion between the components is limited if the components are macroscopically immiscible. In one of the systems (HSCH), the binary fluid may be compressible due to diffusion. In the other system (BHSCH), a Boussinesq approximation is used and the fluid is incompressible. In this paper, we focus on buoyancy driven flow and the Rayleigh-Taylor instability. In the fully nonlinear regime before pinchoff, results from the HSCH and BHSCH models are compared to highly accurate boundary-integral simulations of the classical sharp interface system. In this case, we find that the diffuse interface models yield nearly identical results and we demonstrate convergence to the boundary-integral solutions as the interface thickness vanishes. We find that the break-up of an unstably stratified fluid layer is smoothly captured by both models. The HSCH model seems to be more diffusive than the BHSCH model and predicts an earlier pinchoff time which causes subtle differences between

the two in the pinchoff region. Further, in the limit of zero interface thickness, we find that the effect of compressibility does not vanish at pinchoff. This distinguishes the HSCH model from all others in which compressibility effects are neglected. It may turn out, for example, that characterizing the limiting effect of compressibility at pinchoff may suggest a physically-based selection mechanism for cutting and reconnecting sharp interfaces. Varying the gravitational force and viscosities of the fluids yields different pinchoff times and numbers of satellite drops. Moreover, using the analysis of the linear growth rates from our first paper (Part I [1]), we confirm that the modified HSCH/BHSCH parameters suggested in that work lead to improved agreement with sharp interface results at finite interface thicknesses. Lastly, we also consider a case in which the fluid components are miscible. We find competition between buoyancy, viscous, diffusional and, at very early times, surface tension-like forces.

PACS: 47.20.Bp, 47.20.Gv, 47.20.Hw, 47.20.Ky, 47.20.Ma

I. INTRODUCTION

This is the second paper in a two part series in which we analyze two diffuse interface models to study pinchoff and reconnection in binary fluid flow in a Hele-Shaw cell with arbitrary density and viscosity contrast between the components. In this paper, we focus our analysis on a study of the nonlinear regime including pinchoff and reconnection. In the first paper (Part I [1]), we presented the model equations and studied their equilibria, one dimensional evolution and linear stability.

In a Hele-Shaw cell, viscous fluid lies between two flat parallel plates which are separated by a small gap. In this geometry, the Navier-Stokes equations simplify considerably and the gap-averaged velocity of the fluid is given by Darcy's law. See, for example, the reviews by Homsy [2] and Saffman [3]. In the flow we primarily consider in this paper, an unstably stratified layer of light fluid is surrounded by a heavy fluid. See figure 1 in Part I. The Rayleigh-Taylor instability then drives the break-up of the layer into drops. Such changes in the topology of interfaces are fundamental features of multi-component fluid flows and are still poorly understood as the collision of material surfaces produces a singularity in the fluid equations (e.g. [4]). The relative simplicity of the governing equations makes Hele-Shaw flows natural test cases in which to study this phenomena (e.g. see [5–13]). Indeed, one of the goals of our work is to develop insight that can be used in the study of viscous fluids in more general geometries using diffuse interface models.

There are several ways in which interface transitions may be modeled. In interface tracking algorithms (see e.g. [14–21]) the topology of interfaces is typically changed using ad-hoc cut-and-connect rules. In general, these rules are difficult to justify physically although there are a few special cases in which this may been done using similarity solutions (see [22–24]). In the context of colliding drops, however, Nobari et al. [19] noticed that the flow may sensitively depend on the time at which the interface surgery is performed. In the level set (e.g. see [25–30]) and volume of fluid (e.g. see [31–35] interface capturing algorithms, the numerical viscosity associated with solving the equations of motion provides the mech-

anism by which the topology of interfaces may change smoothly. The flow discontinuities (density,viscosity) are typically smoothed as well although there are now several methods in which the interface jump conditions (i.e. surface tension) are handled explicitly [36–38]. It is not clear, however, which types of smoothing and numerical viscosity are physically justified.

In the (diffuse) interface capturing method that we use in this paper, (chemical) diffusion between the different fluid components provides the physical mechanism to smooth flow discontinuities and to yield smooth evolutions through topology changes; an approach suggested by Goodman et al. [39–41]. The diffusion is limited if the components are macroscopically immiscible and reflects the partial miscibility real fluids always display. Sharp interfaces are replaced by narrow transition layers whose structure becomes important at topological transitions since the distance between interfaces becomes comparable to the interface thickness. While the thickness of interfaces between real immiscible fluids, such as oil and water, may be microscopic, our thicknesses are limited by numerical resolution. Typically, we find that our pseudo-spectral numerical methods require 6 grid cells to resolve the transition layer. Therefore, we pay close attention to the limiting behavior of our results as the interface thickness is reduced in order to estimate their "robustness" with respect to interface thickness.

The idea that interfaces have a finite thickness dates to Poisson [42]. In this approach, an interface between two immiscible fluids may be described as a layer where thermodynamically unstable mixtures are stabilized by weakly non-local terms (gradients) in the energy [43] which have their origins in molecular force interactions between the components [44,45]. These gradient terms induce extra reactive stresses in the fluid which become surface stress in the zero thickness limit. There have been many research efforts in this area and we refer the interested reader to the recent review by Anderson, McFadden & Wheeler [46] and the introduction of Part I [1] for a collection of recent references.

In this paper, we study the nonlinear evolution of unstably stratified fluid layers in a Hele-Shaw (HS) cell, through pinchoff and reconnection, using the diffuse interface models

(HSCH and BHSCH systems) we presented in Part I. These equations are obtained by simplifying a system of general equations of motion for binary fluids, whose components have arbitrary density and viscosity contrast (NSCH model [47]), to the Hele-Shaw case. In the HSCH/BHSCH systems, a concentration field is introduced and evolved. Gradients in concentration generate reactive stresses in the fluid which mimic surface tension. The flow velocity is obtained from a generalized Darcy's law and the concentration field evolves according to a nonlinear, fourth order diffusion equation of Cahn-Hilliard (CH, [48]) type. In the HSCH model, diffusion between different density fluids generates non-solenoidal velocity fields. In addition, the chemical potential depends explicitly on the fluid pressure. In the BHSCH model, density differences are assumed to be small and a Boussinesq limit is taken. In the BHSCH case, the velocity is solenoidal and the chemical potential does not depend on the pressure.

Recently, E & Palffy-Muhoray [49] derived equations similar to the HSCH model to study polymer melts (see also [50]). In addition, Verschueren [52] derived an analogous system to study thermocapillary flow in a Hele-Shaw cell. In the case of density matched components, the HSCH model reduces to one which was previously used by Shinozaki and Oono [51] to study spinodal decomposition and has been recently used by Verschueren [52] to study coalescence in hyperbolic flows. Very recently, Struchtrup & Dold [53] derived a version of the HSCH system to study miscible, buoyantly unstable reaction fronts in a Hele-Shaw cell.

The HSCH and BHSCH models belong collectively to the class of phase-field models which have been widely used for free boundary problems in other physical situations such as the solidification of binary alloys, e.g. see the review edited by Gurtin & McFadden [54]. In fact, because there is a close connection between quasi-steady diffusion and the Hele-Shaw problem (both involve harmonic fields in a domain with a free boundary), some phase-field equations (even the classical Cahn-Hilliard equation), have Hele-Shaw like sharp interface limits (e.g. [55–58]). Typically these limiting models do not include hydrodynamic effects such as buoyancy. Very recently, however, Folch et al. [59] derived, analyzed and implemented numerically a phase-field model for Hele-Shaw flows, also with buoyancy and

arbitrary viscosity contrast, to study the evolution of viscous fingers (e.g. [60]). Their approach differs from ours in several important ways. In their model, a modified Allen-Cahn equation [61] (non-conservative equation) governs the motion of the phase field which is then coupled to a dissipative, time evolution equation for the stream function. While the authors show that this system converges to the classical Hele-Shaw system in the thin interface limit and indeed reproduces fingering, it seems difficult to justify their choice of phase-field function and governing equations from physical considerations. Our approach, on the other hand, is motivated by physical considerations such as chemical diffusion.

In this paper, we investigate the differences between the HSCH, BHSCH and classical sharp interface models in the nonlinear regime. Away from the pinchoff region, both the HSCH and BHSCH models yield nearly identical results and converge to the classical sharp interface model as the interface thickness vanishes. We find that the break-up of an unstably stratified fluid layer is smoothly captured by both the HSCH and BHSCH models. The HSCH model seems to be more diffusive than the BHSCH model and predicts an earlier pinchoff time which causes subtle differences between the two in the pinchoff region. Further, in the limit as the interface thickness is reduced to zero, we find that the effect of compressibility does not vanish at pinchoff. This distinguishes the HSCH model from all others (including that of Folch et al. [59]) in which compressibility effects are neglected. It may turn out, for example, that characterizing the limiting effect of compressibility at pinchoff may suggest a physically-based selection mechanism for cutting and reconnecting sharp interfaces.

Varying the gravitational force and viscosities of the fluids yields different pinchoff times and numbers of satellite drops. Moreover, using the analysis of the linear growth rates from our first paper (Part I [1]), we confirm that the modified HSCH/BHSCH parameters suggested in that work lead to improved agreement with sharp interface results at finite interface thicknesses.

Lastly, we also consider a case in which the fluid components are miscible. We find competition between buoyancy, viscous, diffusional and, at very early times, surface tension-

like forces. In the miscible case, we find that when the unstable stratification of density and viscosity are aligned, fingering analogous to that seen in the immiscible case is observed. Otherwise, diffusion seems to dominate and there is little differential motion of the fluids.

The paper is organized as follows. In section II, the HSCH and BHSCH models are presented and briefly discussed. In section III, the numerical discretization of the systems is described. In section IV, the numerical results are presented. Finally, in section V, conclusions are given.

II. THE HELE-SHAW-CAHN-HILLIARD MODEL

Consider a viscous two-component (binary) fluid between two parallel plates with gap width b (e.g. see figure 1 of Part I). We suppose that the two plates are located at $z = \pm b$ and extend over the region $0 \leq x, y \leq L$ where $\delta = b/L$ is small. Let $c(\mathbf{x}, t)$ be the mass concentration of one of the fluid components (e.g. M_1/M where M_1 is the mass of component 1 and M is the total mass of the binary fluid in a representative volume V). As in Part I, c is always the mass concentration of the fluid labeled 1 (the light fluid). Let ρ_1, ρ_2 and $\mathbf{v}_1, \mathbf{v}_2$ be the densities (M_i/V) and velocities of the two fluid components respectively. Let $\rho = \rho(c)$ be the total density (M/V) and $\mathbf{v}$ be the mass-averaged velocity field, i.e. $\rho\mathbf{v} = \rho_1\mathbf{v}_1 + \rho_2\mathbf{v}_2$.

Separately, the fluid components are assumed to be incompressible and have constant densities and viscosities. We assume that the density of the binary fluid depends on the concentration but not on the pressure. In particular,

$$\frac{1}{\rho(c)} = \frac{1}{\rho_1}c + \frac{1}{\rho_2}(1 - c), \tag{2.1}$$

which implies that volume is preserved under mixing (simple mixture assumption [62]). Diffusion is allowed to occur between the components which is limitied if the components are macroscopically immiscible. The binary fluid is then termed "quasi-incompressible" [47,62,63] since diffusion may introduce density variation and hence may cause the mass-averaged velocity of the binary fluid to be non-solenoidal thus introducing compressibility effects.

In Part I, we presented a simplification, to the Hele-Shaw case, of the general Navier-Stokes-Cahn-Hilliard (NSCH [47]) equations for binary fluids which takes into account the chemical diffusivity between different components of a fluid mixture and the extra fluid stresses induced by inhomogeneity (Van der Waals stresses). In particular, we followed the classical sharp interface model and assumed Poiseuille flow between the plates. In addition, we assumed there is no diffusion in the direction normal to the plates. This results in a generalized Darcy law in which there is only planar flow and diffusion. This yields one of the simplest such systems that can describe the flow and indeed captures topological transitions smoothly (referred to as the HSCH model). However, it does not account for 3-d flow which could play a role near the meniscus and near pinchoff and reconnection. To rule out such effects, one would have to perform a detailed analysis of meniscus region as is done by Park & Homsy [64] for the classical Hele-Shaw model. We did not perform such an analysis (although it seems quite possible such an analysis could be performed at least away from topology transitions) and thus our model should be understood as just that– a model. We do provide an indirect justification for our model by demonstrating that it converges to the classical sharp interface models in the limit of zero interface thickness.

The HSCH model is then given as follows. Let $\mathbf{u}$ be the nondimensional, gap-averaged velocity field. Then,

$$\mathbf{u} = -\frac{1}{12\eta(c)}\left[\nabla q + \frac{\mathbf{C}}{\mathbf{M}}\rho(c)\left(\Delta c \nabla c - \frac{1}{2}\nabla|\nabla c|^2\right) - \tilde{G}\rho(c)\hat{y}\right], \tag{2.2}$$

$$\nabla \cdot \mathbf{u} = -\frac{1}{\rho}\rho'(c)(c_t + \mathbf{u}\cdot\nabla c) = -\frac{\alpha}{\mathbf{Pe}}\Delta_2\mu \tag{2.3}$$

$$\rho(c_t + \mathbf{u}\cdot\nabla c) = \frac{1}{\mathbf{Pe}}\Delta\mu, \tag{2.4}$$

where q is a modified pressure, $\hat{y}$ is a unit vector in the y direction, $\tilde{G}$ is a measure of gravitational force and

$$\alpha = -\frac{\rho'}{\rho^2} = \frac{1}{\rho_1} - \frac{1}{\rho_2}, \tag{2.5}$$

is a constant where ρ_1 and ρ_2 are the densities of the fluid components before mixing. As in Part I, we scale the nondimensional parameters $\mathbf{C}$, $\mathbf{M}$, and $\mathbf{Pe}$ with a single parameter

γ which measures the interface thickness. The following scaling yields the classical sharp interface as a limiting case when $\gamma \to 0$ [1]:

$$\mathbf{C} = \gamma^2, \qquad \mathbf{M} = \tilde{\tau}\gamma, \qquad \mathbf{Pe} = O(1/\gamma). \tag{2.6}$$

In the above, $\tilde{\tau}$ is a scaled surface tension.

The generalized chemical potential μ is given by

$$\mu = \mu_0(c) + \alpha \mathbf{M} q - \mathbf{C}\Delta c, \tag{2.7}$$

where $\mu_0(c) = f_0'(c)$. Note that chemical potential depends explicitly on the fluid pressure. If the fluid components are immiscible, then f_0 is taken to be a nonconvex function of c. If the components are miscible, f_0 is taken to be a convex function of c (e.g. see figure 2 in Part I). Note that for f_0 nonconvex, there is a region (called the spinodal region) in which the diffusion coefficient $f_0''(c) < 0$. This creates anti-diffusion and is what prevents the fluids from mixing completely. The system (2.2)-(2.7) also has the non-increasing energy functional

$$E = \frac{1}{\mathbf{M}} \int_\Omega \rho(c) \left[\left(f_0(c) + \frac{\mathbf{C}}{2} |\nabla c|^2 \right) + \mathbf{M}\tilde{G} y \right] dxdy, \tag{2.8}$$

which is the sum of the dimensionless surface (chemical) and potential energies. We refer the reader to Part I for further details.

The HSCH system is much simpler to solve than the full NSCH equations. In the HSCH model, the velocity, rather than being determined from the balance of linear momentum, instead is given by a generalized version of Darcy's law (2.2) which relates the velocity, viscosity, pressure and concentration. Several essential features of the NSCH model are retained, however. First, the velocity $\mathbf{u}$ is not necessary solenoidal which may introduce compressibility effects. Second, gradients in concentration may produce forces which mimic the effect of surface tension (see Part I). Third, the chemical potential depends explicitly on the fluid pressure. We note that equations similar to (2.2)-(2.7) were derived by E and Palffy-Muhoray in the context of polymer melts [49]. In particular, those authors noticed

the dependence of the chemical potential on the pressure. However, they did not seem to account for compressibility effects due to density differences of the constituents. In addition, Verschueren derived an analogous system to study thermocapillary flow in a Hele-Shaw cell [52].

We also consider a simpler version of the HSCH model obtained using a Boussinesq (B) approximation in which density variation is small but the gravitational force is large. As discussed in Part I, the BHSCH system is obtained by taking the density to be a constant equal to 1 everywhere except in the gravitational term. The BHSCH model is then

$$\mathbf{u} = -\frac{1}{12\eta(c)}\left[\nabla q + \frac{\mathbf{C}}{\mathbf{M}}\left(\Delta c \nabla c - \frac{1}{2}\nabla|\nabla c|^2\right) - \tilde{G}\tilde{\rho}(c)\hat{y}\right], \tag{2.9}$$

$$\nabla \cdot \mathbf{u} = 0 \tag{2.10}$$

$$c_t + \mathbf{u}\cdot\nabla c = \frac{1}{\mathbf{Pe}}\Delta\mu, \tag{2.11}$$

where

$$\tilde{\rho}(c) = (\rho_1 - 1)c + 1, \tag{2.12}$$

and $\rho_2 = 1$. Further,

$$\mu = f_0'(c) - \gamma^2\Delta c. \tag{2.13}$$

In the Boussinesq case, the energy Eq. (2.8) reduces to

$$E = \frac{1}{\mathbf{M}}\int_\Omega \left[f_0(c) + \frac{\mathbf{C}}{2}|\nabla c|^2 + \mathbf{M}\tilde{G}\tilde{\rho}(c)y\right] dxdy, \tag{2.14}$$

The BHSCH system is simpler than the HSCH model in that the velocity is solenoidal and the chemical potential does not depend directly on the fluid pressure. Concentration gradients still may produce non-zero velocities however. The system (2.9)-(2.11) has been used previously to study spinodal decomposition in a Hele-Shaw cell in the absence of gravity [51] and was recently used by Verschueren [52] to study coalescence in hyperbolic flows.

As was shown in Part I, the HSCH/BHSCH models have the classical sharp interface model as a limiting case as $\gamma \to 0$ when the scaling Eq. (2.6) is satisfied. For completeness, we give the classical system here. Let a zero thickness interface Γ separate two fluid immiscible, incompressible components. Then, in each fluid region,

$$\nabla \cdot \mathbf{u}_i = 0, \tag{2.15}$$

$$\mathbf{u}_i = -\frac{1}{12\eta_i}(\nabla p - \tilde{G}\rho_i \hat{y}), \tag{2.16}$$

where $i = 1, 2$ labels the two fluid components. The labeling here is to be understood as follows. The 1 denotes the fluid below the interface (i.e. the direction of gravity) and the 2 one denotes the fluid above the interface (i.e. opposite to the direction of gravity). The boundary conditions on the interface Γ are

$$(\mathbf{u}_1 - \mathbf{u}_2) \cdot \mathbf{n} = 0 \tag{2.17}$$

$$(p_2 - p_1) = \tau\kappa, \tag{2.18}$$

where $\mathbf{n}$ is the unit normal vector to Γ, κ is the curvature and τ is the dimensionless surface tension coefficient. The flow is characterized by the two relevant physical parameters the Bond number $\mathbf{B}$ and the Atwood number $\mathbf{A}$:

$$\mathbf{B} = \tilde{G}(\rho_2 - \rho_1)/\tau, \quad \text{the Bond number,} \tag{2.19}$$

$$\mathbf{A} = \frac{\eta_2 - \eta_1}{\eta_1 + \eta_2}, \quad \text{the Atwood number.} \tag{2.20}$$

Therefore, $\mathbf{B} < 0$ means the interface is unstably density stratified (gravity is in the negative y direction). If $\mathbf{A} < 0$ then the viscous stratification is unstable if fluid 2 moves into fluid 1 ($\mathbf{B} < 0$).

To match the surface tension τ of the sharp interface model, the scaled surface tension in the HSCH system must be taken to be

$$\tilde{\tau} = \tau \left[\sqrt{2}\int_{c_2}^{c_1} \rho(c)\sqrt{f_0(c) - f_0(c_1) - f_0'(c_1)(c - c_1)}\; dc\right]^{-1}, \tag{2.21}$$

where $c_{1,2}$ are the equilibrium concentrations of fluid 1 in the two " macroscopically homogeneous" fluid domains (i.e. wells of the non-convex Helmholtz free energy $f_0(c)$, immiscible case). Note that this implies $c_1 \approx 1$ and $c_2 \approx 0$. In what follows, we take the quartic polynomial

$$f_0(c) = c^2(1-c)^2 \tag{2.22}$$

as a simple model for f_0. In the (periodic) geometry we consider in this paper, we found that this choice of f_0 yielded essentially the same results as more complicated logarithmic models (see also Part I). We note that for the free energy in Eq. (2.22), $c_1 = 1$ and $c_2 = 0$ and

$$\tilde{\tau} = \tau 3\sqrt{2}. \tag{2.23}$$

In the remainder of the paper, we take the following conventions. We fix $\tau = 1/(3\sqrt{2})$ so that $\tilde{\tau} = 1$. We then vary the Bond number $\mathbf{B}$ by choice of gravitational constant through Eq. (2.19).

$$\tilde{G} = \frac{\mathbf{B}}{3\sqrt{2}\,(\rho_2 - \rho_1)}. \tag{2.24}$$

Unless otherwise specified, we take the nondimensional parameters as in Eq. (2.6) with $\mathbf{Pe} = 1/\gamma$.

Before we close this section, we present a relatively simple form for the out of plane vorticity ω in the HSCH model, i.e. $\omega = \nabla \times \mathbf{u} \cdot \mathbf{e}_3$ where $\mathbf{e}_3$ is the unit vector out of the plane. The vorticity is given by

$$\omega = -\nabla\left(\frac{\rho(c)}{12\eta(c)}\right) \times \nabla\left(g + \tilde{G}y\right) \cdot \mathbf{e}_3 + \frac{1}{\mathbf{M}}\nabla\left(\frac{\mu\rho(c)}{12\eta(c)}\right) \times \nabla c \cdot \mathbf{e}_3. \tag{2.25}$$

The first term on the right hand side is the baroclinic vorticity and the second term is the vorticity due to surface tension. An analogous formula holds in the BHSCH case.

III. NUMERICAL METHODS FOR THE HSCH EQUATIONS

In this section, we describe the numerical methods used for computing the solutions of the full HSCH model. When appropriate, we point out the simplifications that may be made for simulations of the BHSCH model. Our discussion of the numerical algorithm proceeds as follows. We first present the temporal discretization of Eq. (2.4). We then give the algorithms for the pressure solver and velocity evaluation.

We assume 2π periodicity in both the x and y directions and Fourier pseudospectral methods [65] are used to obtain the spatial discretizations: all spatial derivatives are performed in Fourier space with the Fast Fourier Transform (FFT), while algebraic operations are performed in physical space. No numerical filtering is used.

A balancing pressure

$$q_b = - < \rho > \tilde{G} y, \quad \text{where} \quad < \rho >= \frac{1}{4\pi^2} \int_{[0,2\pi]^2} \rho \, dxdy, \tag{3.1}$$

is added to the model to ensure the fluid pressure q is periodic. More specifically, q in Eq. (2.2) is replaced by $q + q_b$. The BHSCH model is analogously modified. The balancing pressure can also be viewed as arising from changing a stationary reference frame to a moving reference frame which is appropriate to match classical boundary integral simulations of the sharp interface model (see e.g [12,8]).

A. Time Discretization

To integrate the concentration equation (2.4) in time, we use a 3rd order accurate, equilibrium preserving version of a linear propagator method. By equilibrium preserving, we mean that the balance of terms in equilibrium on the continuous level is preserved exactly on the discrete level. Such methods based on an integrating factor (linear propagator) approach were apparently first derived in [66,67].

Following section 4.2 in Part I, let us reformulate Eq. (2.4) using the volume fraction ϕ as the unknown variable instead of c. Recall the transformation between the two is:

$$\phi = \rho(c)c. \tag{3.2}$$

The inverse transformation is

$$c = \phi/\rho(\phi), \quad \text{where} \quad \rho(\phi) = \rho_2(1 - \alpha\phi) \tag{3.3}$$

and α is defined as in Eq. (2.5).

We then obtain the following conservation equation for ϕ:

$$\phi_t = -\frac{\mathbf{C}}{\rho_1 \mathbf{Pe}} \Delta^2 \phi + CN, \tag{3.4}$$

where

$$CN = -\nabla \cdot (\phi \mathbf{u}) + \frac{1}{\mathbf{Pe}} \Delta(\mu_0(c) + \alpha \mathbf{M} q - \mathbf{C} \Delta(c - \frac{\phi}{\rho_1})), \tag{3.5}$$

and we have added and subtracted the term $\frac{\mathbf{C}}{\rho_1 \mathbf{Pe}} \Delta^2 \phi$ to take advantage of the fact that $c - \frac{\phi}{\rho_1}$ is nearly zero away from transition regions. This is because $c \approx 0$ in region 2 since $c_2 = 0$. Note that in the BHSCH model, $\phi = c$ and $\alpha = 0$ in Eq. (3.5) since $\rho = 1$ except in the gravity term.

In the classical linear propagator algorithm (e.g. see [12]), the highest order linear term is integrated exactly in Fourier space. Here, this term is the 4th order diffusive term $-\frac{\mathbf{C}}{\rho_1 \mathbf{Pe}} \Delta^2 \phi$. For illustrative purposes, let us consider a classical linear propagator method applied to Eq. (3.4). The scheme is derived as follows. Take the Fourier transform of Eq. (3.4) and multiply by the integrating factor e^{mt}, where

$$m = \frac{1}{\rho_1} \frac{\mathbf{C}}{\mathbf{Pe}} |\mathbf{k}|^4$$

and $\mathbf{k} = (k_1, k_2)$ is the Fourier wavenumber vector. This yields an ODE in time at each wavenumber:

$$(e^{mt} \hat{\phi})_t = e^{mt} \hat{CN}. \tag{3.6}$$

Discretizing Eq. (3.6) in time using the 3-step Adams-Bashforth method (AB3) yields the linear propagator method (LPAB3):

$$\hat{\phi}_{n+1} = e^{-m\Delta t} \hat{\phi}_n + \frac{\Delta t}{12} (23 e^{-m\Delta t} \widehat{CN}_n - 16 e^{-2m\Delta t} \widehat{CN}_{n-1} + 5 e^{-3m\Delta t} \widehat{CN}_{n-2}). \tag{3.7}$$

The 3-stage Runge-Kutta method (RK3) may be used to initialize LPAB3 for example.

The linear propagator method LPAB3 has the nice features of being both explicit and exponentially damping at high wavenumbers in Fourier space. The latter property makes the algorithm quite stable and removes high order time step stability constraints due to the 4th order term. However, it is easy to see that the continuous equilibrium condition

$$m\hat{\phi} = \widehat{CN} \tag{3.8}$$

is not satisfied by the discrete equilibrium. We therefore say that LPAB3 is not equilibrium preserving. Below, we show that one consequence of this is that oscillations are produced in the chemical potential μ.

To overcome this difficulty, we derive a modified linear propagator method (MLPAB3) which preserves Eq. (3.8) for discrete equilibrium. Let [ ] denote an approximation for the quantity inside the bracket. We modify Eq. (3.7) as

$$\hat{\phi}_{n+1} = \frac{\hat{\phi}_n}{[e^{m\Delta t}]} + \Delta t\ (A[e^{-m\Delta t}]\widehat{CN}_n + B[e^{-2m\Delta t}]\widehat{CN}_{n-1} + C[e^{-3m\Delta t}]\widehat{CN}_{n-2}), \tag{3.9}$$

where the approximations and the constants A, B and C are to be determined. In view of Eq. (3.8), we obtain the consistency relation

$$1 - \frac{1}{[e^{m\Delta t}]} = m\Delta t(A[e^{-m\Delta t}] + B[e^{-2m\Delta t}] + C[e^{-3m\Delta t}]) \tag{3.10}$$

for the MLPAB3 method. For simplicity, we set

$$[e^{-2m\Delta t}] = e^{-2m\Delta t}, \qquad [e^{-3m\Delta t}] = e^{-3m\Delta t}.$$

We may then consider a fourth order approximation for $[e^{-m\Delta t}]$

$$[e^{-m\Delta t}] = \frac{1 + m\Delta t + \frac{1}{2}(m\Delta t)^2 e^{m\Delta t/3}}{1 + 2m\Delta t + \frac{1}{2}(2m\Delta t)^2 e^{2m\Delta t/3}} \tag{3.11}$$

and determine $[e^{m\Delta t}]$ by (3.10). Alternatively, we may take the following fourth order approximation for $[e^{m\Delta t}]$

$$[e^{m\Delta t}] = \frac{e^{m\Delta t}}{e^{m\Delta t} - m\Delta t(1 + \frac{1}{2}m\Delta t e^{\frac{1}{3}m\Delta t})} \tag{3.12}$$

and determine $[e^{-m\Delta t}]$ using (3.10). In the former approach, $[e^{-m\Delta t}]^{-1}$ damps modes at large wave number exponentially but $[e^{m\Delta t}]$ damps only algebraically, and vice versa in the latter approach. Our numerical experiments show that the computations are better resolved when we have exponental damping on CN, and so we shall use (3.11). Moreover, it is easy to check that the same constants as in (3.7)

$$A = \frac{23}{12}, \quad B = -\frac{16}{12}, \quad B = \frac{5}{12}$$

make the MLPAB3 method 3rd order accurate in time.

One of our motivations for using an equilibrium preserving time integration method for the HSCH and BHSCH models is that away from pinchoff and reconnection, the chemical potential μ should be nearly in local equilibrium as seen from the sharp interface asymptotics in Part I. That is, μ should be nearly constant across the transition region. This is especially important in the HSCH model because the mass conservation equation (2.3) links $\nabla \cdot \mathbf{u}$ with $\Delta\mu$.

To see the implications of equilibrium preservation, in figure 2 we plot a slice of the HSCH chemical potential $\mu(x = \pi, y, t = 0.5)$ using the LPAB3 (dashed curve) and MLPAB3 methods (solid curve) for time integration. Observe that unphysical oscillations are produced at the interfaces when the LPAB3 method is used. Because they are amplified through the evolution, the oscillations eventually cause the solution $c(\mathbf{x}, t)$ to become inaccurate. The chemical potential from the MLPAB3 method, on the other hand, remains smooth and the corresponding solution $c(\mathbf{x}, t)$ remains accurate for long times. In this simulation, the initial condition is given in Eqs. (4.1) and (4.2) with $k = 1$ and $\epsilon = 0.1$ (see figure 1(a) for a schematic of the initial condition). The Atwood number $\mathbf{A} = 0$ and the viscosity $\eta(c) = 1/2$. the Bond number $\mathbf{B} = -25$ for the upper interface and $\mathbf{B} = 25$ for the lower interface. The spatial grid size is $h = 2\pi/N$ with $N = 256$ (there are approximately six grid points across the interface layer, see figure 1(b)) and the time step is $\Delta t = 0.001$. Finally, the algorithms for the pressure solver and velocity evaluation are given below.

B. The Pressure Solver

For the HSCH model, the pressure equation is obtained by taking the divergence of Eq. (2.2) and using Eq. (2.3). This gives

$$\nabla \cdot [(\frac{\alpha^2 \mathbf{M}}{\mathbf{Pe}} + \frac{1}{12\eta(c)})\nabla q] = -\frac{\alpha}{\mathbf{Pe}}\Delta(\mu_0(c) - \mathbf{C}\Delta c) - \nabla \cdot \left[\frac{1}{12\eta(c)}\left\{\frac{\mathbf{C}}{\mathbf{M}}\rho(\Delta c \nabla c - \frac{1}{2}\nabla|\nabla c|^2) - \tilde{G}\rho(c)\hat{y}\right\}\right] \qquad (3.13)$$

In addition, we use the explicit cancellation

$$\nabla \cdot (\Delta c \nabla c - \frac{1}{2}\nabla(|\nabla c|^2)) = 2(c_{xx}c_{yy} - c_{xy}^2)$$

to improve the resolution of the numerical solution. Eq. (3.13) is solved simply by inverting the Laplacian in the constant viscosity case in Fourier space using the FFT or by using the conjugate gradient method in the variable viscosity case. An analogous pressure equation is obtained for the BHSCH model.

C. The Velocity Evaluation

In the HSCH model, the velocity $\mathbf{u}$ is not divergence free. From Eq. (2.3), we obtain the following orthogonal decomposition for $\mathbf{u}$:

$$\mathbf{u} = \frac{\alpha}{\mathbf{Pe}}\nabla\mu + \nabla^{\perp}\psi, \tag{3.14}$$

where the first term on the right hand side is the potential function and ψ is the stream function. Further,

$$\nabla^{\perp} = (\frac{\partial}{\partial y}, -\frac{\partial}{\partial x}).$$

When the viscosity η is a constant, ψ is a periodic function since the right hand side of Eq. (2.2) has zero mean. If η is non-constant, then ψ contains a linear term in $\mathbf{x}$. In the non-constant case, we evaluate $\mathbf{u}$ via Eq. (2.2). In the constant case, we use ψ where

$$\Delta\psi = -\frac{1}{12\eta}(\frac{\mathbf{C}}{\mathbf{M}}\nabla^{\perp}(\rho(\Delta c \nabla c - \frac{1}{2}\nabla|\nabla c|^2) - \tilde{G}\nabla^{\perp}(\rho\hat{y})). \tag{3.15}$$

Note that the negative of the right hand side of Eq. (3.15) is the vorticity of the fluid (in the constant η case). We also use the cancellation

$$\nabla^{\perp}(\Delta c \nabla c) = (\Delta c)_y c_x - (\Delta c)_x c_y \tag{3.16}$$

to improve resolution of numerical solutions. Eq. (3.15) is solved by inverting the Laplacian in Fourier space using the FFT. The velocity in the BHSCH model is obtained analogously.

IV. NUMERICAL RESULTS

In this section, we present numerical results for the full HSCH and BHSCH models. In particular, we consider a specific type of flow geometry: an unstably stratified layer of light fluid surrounded by a heavy fluid (see figure 1). The specific initial data we consider take the following form. Let the curves $(x, y_1(x,0))$ and $(x, y_2(x,0))$ be the centerlines of the diffuse interface and take

$$y_1(x,0) = \pi - (0.5 + \epsilon\cos(kx)), \qquad y_2(x,0) = \pi + (0.5 + \epsilon\cos(kx)), \quad 0 \le x \le 2\pi, \quad (4.1)$$

where k denotes the wavenumber of the perturbation from the horizontal y_i = constant. Then, the initial concentration field $c(x,y,0) = c_0(x,y)$ is given by

$$\begin{aligned} c_0(x,y) = \frac{1}{4}(1 + \tanh((y - y_1(x))/(2\sqrt{(}\mathbf{C}/2)))) \\ * \ (1 - \tanh((y - y_2(x))/(2\sqrt{(}\mathbf{C}/2)))). \end{aligned} \quad (4.2)$$

An example of the evolution we wish to capture is given in figure 3 where a simulation of the sharp interface model (2.15)-(2.18) is shown. The non-stiff boundary integral method of [12] is used to solve the equations. The initial interface positions are as in Eq. (4.1) with $k = 1$ and $\epsilon = 0.1$. In this simulation, the interface is periodic in the x-direction and periodicity in the y-direction is simulated by having two additional layers of light fluid included in the calculation (not shown), each a distance of 2π above and below the layer shown. We found including more such layers did not change the results significantly. The Bond numbers of the upper and lower interfaces are $\mathbf{B} = -25$ and $\mathbf{B} = 25$ respectively. The surface tension is $\tau = 1/(2\sqrt{3})$ for each interface and the viscosities are matched with $\eta_1 = \eta_2 = \eta = 1/2$ ($\mathbf{A} = 0$).

From the figure, we see that the upper interface is unstable and the heavy fluid fingers through the layer of light fluid. The lower interface is stable and hence resists motion. Eventually, the finger of heavy fluid breaks through the layer at time $t = t_c$ ($t_c \approx 7.5$). At this time, a singularity forms in the sharp interface model and the simulation is halted.

This type of topological transition has been extensively studied by Goldstein, Pesci & Shelley [8–11]. In their work, the authors analyze a lubrication approximation of the sharp interface model and obtain approximations of the singularity time t_c and asymptotic pinchoff shape which match very well those seen in simulations of the full equations. Here, rather than focusing on the singularity, we wish to go beyond it. In particular, from figure 3, it seems likely that the periodic layer breaks into a sequence of large bubbles and small satellite drops. As we see next, this is indeed what occurs in the HSCH and BHSCH models.

A. Beyond Break-up

Let us now use HSCH and BHSCH models to simulate the flow indicated in figure 3. In the BHSCH case, the initial condition for $c(\mathbf{x}, t)$ is that given in Eqs. (4.2) and (4.1) with y_1 and y_2 as in the sharp interface simulation. $\mathbf{B}$, $\mathbf{A}$, η and τ are matched to the sharp interface values. In the HSCH case, the initial data for c was actually locally equilibrated by solving the pure Cahn-Hilliard equation for the short time interval $0 \leq t \leq 10^{-2}$ with time step $\Delta t = 10^{-6}$ using the data described above as the initial condition. This is done to reduce the effects of non-equilibrium $c(\mathbf{x}, t)$ on $\nabla \cdot \mathbf{u}$ via Eq. (2.3). In the BHSCH case, we checked that equilibrating the initial data had no discernible affect on the results. In the HSCH model, the density ρ is given by Eq. (2.1) with $\rho_2 = 1$ and $\alpha = 0.1$. In the BHSCH model, the density $\tilde{\rho}$ is taken to be $\tilde{\rho}(c) = 1 - \alpha_g c$ with $\alpha_g = 0.091$ so that the density difference matches that in the HSCH and sharp interface models.

In figures 4 and 5, the evolution of $c(\mathbf{x}, t)$ contours is shown for the HSCH and BHSCH models respectively. The contour levels are uniformly spaced from 0.1 to 0.9. In these simulations, the interface thickness parameter is $\gamma = 0.04$, the grid size in each direction is $h = 2\pi/N$ with $N = 256$ and the time step is $\Delta t = 1 \times 10^{-3}$. There are approximately 6 grid points across each interface layer.

The flow evolution is quite similar to that observed in the sharp interface case; this is made more precise below. The thickness of the transition layers is clearly seen and is nearly

uniform in time. Further, the HSCH and BHSCH models are able to smoothly capture the pinchoff of the light layer of fluid. Both models predict that the small satellite drop, produced by the initial pinchoff, later breaks up to form three smaller drops which circularize due to surface tension. The mechanism for break-up is the diffusion between components which becomes important when the distance between the upper and lower interfacial layers becomes comparable to the interface thickness itself. See time $t = 7.5$ for example. Before pinchoff, the HSCH and BHSCH models yield virtually indistinguishable results. At pinchoff and beyond, small differences occur due to the effects of compressibility; we defer discussion of this until the next subsection.

Although pinchoff is not well-defined, since the interface has a finite thickness, it is natural to define pinchoff with respect to the topology of the layer centerline $c = 1/2$. This is consistent with the sharp interface asymptotics where the layer centerline is identified with the sharp interface. With this in mind, consider figure 6 which shows the evolution of the $c = 1/2$ contour line, together with several vorticity contours, for the HSCH model. The graphs for the BHSCH model are analogous. In this figure, the $c = 1/2$ contour is the dotted curve. The solid curves indicate the $\omega = 0.25 \cdot \omega_{max}$ and $\omega = 0.75 \cdot \omega_{max}$ contours (positive vorticity) and the dashed curves show the $\omega = 0.25 \cdot \omega_{min}$ and the $\omega = 0.75 \cdot \omega_{min}$ contours (negative vorticity). A close-up of the region near the satellite drops is shown at the bottom of the figure.

The initial pinchoff of the $c = 1/2$ contour is seen to occur once the thickness of the light layer of fluid becomes on the order of the interface thickness. This happens between $t = 7.5$ and $t = 8.0$ (actually at $t = 7.65$ in the HSCH case and $t = 7.7$ in the BHSCH case; see figure 10). There is also a secondary pinchoff at $t \approx 8.5$.

The evolution and structure of the vorticity is also quite interesting. Before pinchoff, the largest absolute values of ω occur on the sides of the penetrating finger of heavy fluid and are due to buoyancy (baroclinic vorticity). Near pinchoff, light fluid streams from the neck regions into the larger bubbles and the highest values of the vorticity occur in the neck due to surface tension. At pinchoff, surface tension creates oppositely-signed vorticity

at the tips of the satellite drop. This can be seen at time $t = 8.0$ where the vorticity on the upper interface of the thin satellite drop has the opposite sign as its counterpart before pinchoff (e.g. compare at $t = 7.0$; also see the bottom plot in the figure). This vorticity causes the tip of the satellite drop to rebound. At $t = 8.0$, the largest vorticity is still associated with the large, rising bubbles of light fluid. This vorticity, also due to surface tension, causes the tips of these bubbles to rebound and be drawn towards the bulk region thereby reducing curvature (and interface length). The vorticity decays once the curvature of the tip is reduced. At $t = 8.5$, the largest vorticity is now associated with the pinchoff of the thin satellite drop into three smaller drops. The structure of this secondary pinchoff is analogous to that of the original transition.

The vorticity, in fact, can be used to identify the transition. As seen in figure 7(a), the maximum of the vorticity $\omega_m(t) = \max_{\mathbf{x}} |\omega(\mathbf{x}, t)|$ achieves its largest values at pinchoff. This plot shows $\omega_m(t)$ for the HSCH model with several different interface thicknesses. The BHSCH result is analogous. As seen from this figure, there is peak of $\omega_m(t)$ at $t \approx 7.8$ due to the initial pinchoff. Consequently, the pinchoff time may also be defined as the time at which the peak vorticity occurs. In the $\gamma = 0.04$ and $\gamma = 0.05$ cases, there is an additional peak corresponding to the secondary pinchoff. There is only a single peak in the $\gamma = 0.08$ and $\gamma = 0.06$ cases because there is no secondary pinchoff due to the diffuseness of the interface for those values of γ. In addition, observe that ω_m is an increasing function of γ. Indeed, the vorticity in the sharp interface case is a delta function supported on the interface. In the HSCH (and BHSCH) case, we find that ω_m scales with $1/\gamma$. This is shown in figure 7(b) where $\gamma \cdot \omega_m(t)$ is plotted for several interface thicknesses. Note the collapse of the curves before and after pinchoff. Although we do not present it here, we find that before and after pinchoff, the vorticity off the interface is a decreasing function of γ. Since the interface thickness is $O(\gamma)$, this suggests that the HSCH (and BHSCH) vorticity converges to a delta function before and after pinchoff. At pinchoff, the vorticity is more singular, consistent with singularity formation in the classical sharp interface model.

In figure 7(c), we compare the maximum vorticity due to surface tension ('o' curve)

with $\omega_m(t)$. Observe that baroclinic vorticity is dominant until pinchoff. Near pinchoff, the vorticity due to surface tension dominates.

Now let us investigate the effect of the interface thickness parameter on the flow evolution. We begin by considering the effect of γ on the secondary pinchoff. This may be seen in figure 8 which shows the contours of c at time $t = 8.5$ for $\gamma = 0.04$, 0.05, 0.06 and 0.08. As γ decreases, the interface becomes thinner and the small satellite drops are better resolved. On this scale, it is seen that γ has only a small effect on the large bubbles. Upon closer examination, it may be seen that the bubbles actually rise higher as γ is decreased.

Let us now obtain a direct measurement of the effect of γ on the interface position. Recall that $\gamma = 0$ corresponds to the sharp interface model. In figure 9(a), the sharp interface (solid) at $t = 7.5$ is plotted together with the $\gamma = 0.04$ (dashed), 0.05 (dash-dot) and 0.06 (dotted) $c = 1/2$ contours from the HSCH model. As γ is reduced, the $c = 1/2$ contours tend towards the sharp interface. To quantify this, consider the intersection of the curves with the y-axis. Let y_γ be the y-intercept of the upper interfaces with thickness γ. Then, assuming

$$y_\gamma = y_0 + y_p \gamma^p, \tag{4.3}$$

we find $p \approx 1.031$. Thus, the convergence is approximately linear which is consistent with the sharp interface asymptotics from Part I. This is demonstrated in figure 9(b) where the difference $y_0 - y_\gamma$ is plotted versus γ.

Next, let us examine the situation after pinchoff. Consider the flow at $t = 8.0$. Since this is after pinchoff, there is no longer a classical sharp interface with which to compare. Therefore, we consider only the HSCH $c = 1/2$ contours. These contours are shown in figure 9(c). Considering the y intercept as before, we find that y_γ satisfies Eq. (4.3) with $p \approx 1.0375$ and $y_0 \approx 5.82$. This is shown in figure 9(d) which suggests linear convergence to a sharp interface after pinchoff. We note that more rapid convergence is observed at the lower regions of the large bubbles and at the upper and lower regions of the satellite drops. Convergence is approximately linear at the drop tips.

Since our results suggest convergence of the HSCH/BHSCH models to a sharp interface after pinchoff, it is natural, in view of our asymptotic analysis, to expect that the classical sharp interface equations govern its motion. However, what remains to be determined is the transition. In particular, what clues do the HSCH/BHSCH models give as how to connect the classical sharp interface models through pinchoff? We follow-up this question in the next section when we discuss the effect of compressibility at pinchoff. However, we are not yet able to derive topological jump conditions from the HSCH/BHSCH models to pinchoff and reconnect sharp interfaces.

B. Compressibility

We begin our discussion of compressibility by comparing the results from the HSCH and BHSCH models near pinchoff. In figure 10, the $c = 1/2$ contours for the HSCH (solid) and BHSCH (dashed) are shown at several times close to pinchoff. Also plotted are the vectors of the velocity difference $\mathbf{u}_{HSCH}$-$\mathbf{u}_{BHSCH}$. In this simulation, we use $\Delta t = 10^{-4}$ to make our time integration highly accurate. All other parameters are as before.

At $t = 7.5$, the $c = 1/2$ contours of the two models are nearly identical. The vectors, however, indicate that fluid in the HSCH model is flowing faster in the pinchoff region and we see that pinchoff occurs in the HSCH model slightly earlier than it does in the BHSCH case. The differences observed between the results of the two models are confined to the pinchoff region.

To better understand the source of the differences, consider $\nabla \cdot \mathbf{u}$ for the HSCH model near pinchoff. In figure 11, several contours of $\nabla \cdot \mathbf{u}$ are shown at $t = 7.6$, together with the $c = 1/2$ contour (dotted). The solid curves correspond to the $(0.25, 0.5, 0.75) \cdot \max(\nabla \cdot \mathbf{u})$ contours (positive) and the dashed curves correspond to the analogous negative contours. Observe that the light fluid in the neck region is compressed. This makes sense since

$$\nabla \cdot \mathbf{u} = \frac{\alpha}{\mathbf{Pe}} \Delta \mu = -\frac{D}{Dt} \log \rho(\mathbf{x}, t) \tag{4.4}$$

in the HSCH model and ρ is increasing in the neck region due to diffusion; D/Dt is the advective time derivative. The compression apparently allows the layer to become slightly narrower earlier than in the BHSCH model enhancing diffusion and pinchoff.

Let us now determine which terms are dominant in the chemical potential μ and hence contribute most to $\nabla \cdot \mathbf{u}$. To do this, consider a slice of the data at time $t_* = 7.7$ where the slice is taken at $x = x_*$ where the $\max |\nabla \cdot \mathbf{u}|$ is achieved. The slices are shown in figure 12. In (a), the concentration is shown. The peak corresponds to the interior of the pinching region. In (c) and (d), the chemical potential μ and $\nabla \cdot \mathbf{u}$ are shown respectively. The peaks (and valleys) again correspond to the pinchoff region. In (b), the components of μ are indicated. The $\mu_0(c)$ component is the solid curve, the $\mathbf{C}\Delta c$ component is the dashed curve and the $\alpha \mathbf{M} q$ component is the dot-dashed curve. Clearly, the concentration components of μ are dominant; the pressure contribution is seen to be small and slowly varying even through the pinchoff region. This suggests that for this flow, the pressure dependence of the chemical potential is rather weak and the compressibility of the fluid is mainly due to the variation in $c(\mathbf{x}, t)$ from diffusion.

Not surprisingly, the temporal behavior of $\nabla \cdot \mathbf{u}$ is reminiscent of that of the vorticity. In particular, the magnitude of $\nabla \cdot \mathbf{u}$ is large only near the pinchoff time. This is shown in figures 13(a) and (b). From these graphs, we see that near pinchoff, the magnitude of $\nabla \cdot \mathbf{u}$ is an increasing function of γ.

To determine the γ scaling of $\nabla \cdot \mathbf{u}$, consider the previously defined slice of $\nabla \cdot \mathbf{u}$ for several different values of γ. The slices are given in figure 14. In each case, we evaluate the integral

$$I_\gamma = \int_{\{y | \nabla \cdot \mathbf{u}(x_{*,\gamma}, y, t_*) < 0\}} \nabla \cdot \mathbf{u}(x_{*,\gamma}, y, t_*) \, dy. \tag{4.5}$$

We find that $I_{0.06} = -0.0162$, $I_{0.05} = -0.0178$ and $I_{0.04} = -0.0217$. This suggests that $\nabla \cdot \mathbf{u} \neq 0$ *persists* in the limit as $\gamma \to 0$ at the pinchoff time. We also checked that a two dimensional version of the above integral centered about the pinchoff point is non-vanishing at the pinchoff time as well. Since compressibility seems to persist in the zero-thickness

limit, compressibility at pinchoff may provide a physically-based selection mechanism for reconnecting sharp interfaces after pinchoff.

While compressibility appears to affect the flow near the pinchoff region, the bulk flow is relatively insensitive to the presence of compressibility. This is to be expected since pinchoff is a local phenomenon and we have shown that compressibility is only important at pinchoff. What is perhaps surprising is that the details of the pinchoff region are quite similar for the HSCH and BHSCH models, albeit with a time shift due to the fact that pinchoff occurs earlier for the HSCH model. For example, the number and shapes of the satellite drops appear to be rather insensitive to the effects of compressibility. This is likely due to the viscosity-dominant nature of Hele-Shaw flow since highly viscous fluids tend to resist motion. In view of sensitivity of drop evolution to different enforced coalescence times observed in [19], it is likely that flows with significant inertia are much more sensitive to the pinchoff process.

We conclude this subsection by examining the effect of density variation but keeping the Bond number $\mathbf{B}$ fixed; the BHSCH model is one example of doing this in the limit of very small density differences. Let us consider what happens for larger density differences by varying α. Consider the HSCH model with $\alpha = 0.2$ and $\alpha = 0.05$. All other parameters (except for $\tilde{G}$) are as before. From Eq. (4.4), we see that increasing α leads to increasing the compressibility of the flow. In figure 15, the evolution of the $c = 1/2$ contours is shown for the HSCH model. Because of symmetry, only approximately one half of the layer is plotted. The solid curves correspond to $\alpha = 0.05$ and the dashed to $\alpha = 0.2$. Consistent with our previous observations, we see that there is little difference between the two cases except near the pinchoff region. Pinchoff takes place earlier for the larger value of α. Note that the satellite drop at $t = 8.0$ with $\alpha = 0.2$ seems to contain slightly less fluid than the $\alpha = 0.05$ drop. This is due to enhanced diffusion associated with increasing α and is consistent with the linear stability results presented in Part I.

C. Bond Number Variation

Let us now examine the effect of Bond number on the evolution using the HSCH model. Analogous results are obtained for the BHSCH model and are not presented here. In figure 16, the resulting $c = 1/2$ contours for the HSCH model are shown. The leftmost column shows an evolution sequence for $|\mathbf{B}| = 15$ (upper interface has $B = -15$ and lower has $B = 15$), the middle sequence shows $|\mathbf{B}| = 25$ (which is analyzed previously) and the rightmost column shows $|\mathbf{B}| = 35$. The times at which the contours are plotted are different for each choice of $\mathbf{B}$ and are chosen so that the common stages of evolution may be roughly compared. All other parameters are unchanged from their values given in the previous subsection.

As expected, increasing $\mathbf{B}$ makes the flow evolve more rapidly and also changes the number of the satellite drops produced by pinchoff. Two satellites are produced with $\mathbf{B} = 15$, three form with $\mathbf{B} = 25$ and four are present with $\mathbf{B} = 35$. The first satellite drop seen at times $t = 13.1$, 8.0 and 5.8 increases in extent as $\mathbf{B}$ increases. This allows more satellite drops to form by subsequent pinchoffs at larger values of $\mathbf{B}$.

To further characterize the flows, consider $\omega_m(t)$ defined as before. This is shown in figure 17 for the HSCH model; the BHSCH result is analogous. The characteristic peaks of vorticity corresponding to pinchoff are seen. In the $\mathbf{B} = 35$ simulation, there is actually a third peak which is associated with a third pinchoff at $t \approx 6.4$.

As we mentioned previously, one may also define pinchoff to occur when the vorticity reaches a maximum. With this definition and letting $t_{c,\mathbf{B}}$ denote the pinchoff time with Bond number $|\mathbf{B}|$, we find that $t_{c,15} = 12.84$, $t_{c,25} = 7.72$ and $t_{c,35} = 5.54$ for the different Bond numbers. Observe that

$$\frac{t_{c,25}}{t_{c,15}} = 0.6012 \approx \frac{15}{25}, \quad \frac{t_{c,35}}{t_{c,25}} = 0.7176 \approx \frac{25}{35}, \quad \frac{t_{c,35}}{t_{c,15}} = 0.4314 \approx \frac{15}{35}, \tag{4.6}$$

which suggests that the pinchoff times are inversely proportional to the Bond number.

D. Viscosity Variation

Let us now consider the case in which the light and heavy fluids have different viscosities. This introduces an additional source of instability through the displacement of a more viscous fluid by a less viscous one (see e.g. [2]). Here, the displacing force is buoyancy.

For simplicity, we assume that the viscosity is a linear function of concentration and so we set

$$\eta(c) = \eta_1 c + \eta_2,$$

where the numbering is again as indicated in figure 1. We investigate two cases. In the first: (i). $\eta_1 = 0.125$ and $\eta_2 = 0.5$ (Atwood number for upper interface is $\mathbf{A} = 0.6$). In this case, the viscous and gravitational instabilities are misaligned. In the second: (ii). $\eta_1 = 0.5$ and $\eta_2 = 0.125$ and the two instabilities are aligned (Atwood number for upper interface is $\mathbf{A} = -0.6$). The evolution of the HSCH $c = 1/2$ contours for these flows is shown in figure 18; the BHSCH results are analogous. The interface thickness $\gamma = 0.05$ and all other parameters are as in section IV A.

The leftmost column in the figure shows the results for the viscosity matched case $\eta = 1/2$ for comparison. The results of cases (i) and (ii) are graphed in the center and rightmost columns respectively. In both (i) and (ii), the initial pinchoff occurs earlier than in the viscosity matched case due to lowered resistance to motion of the less viscous fluid. Due to the alignment of the viscous and gravitational instabilities, the finger of penetrating heavy fluid shows more deformation in case (ii) than in case (i). One consequence of this is that a satellite drop forms in case (i) and not in case (ii) since the pinchoff region is wider and flatter in case (i).

E. Modified Parameters for the HSCH/BHSCH Models

In this section, we show that the agreement between the HSCH/BHSCH and sharp interface models may be improved at finite interface thicknesses γ by appropriately modifying the

Bond number, and hence gravity via Eq. (2.24), by an amount approximately proportional to γ. In particular, we take the modified Bond number $\mathbf{B} = \mathbf{B}_0(1 + b_{k,\gamma} \cdot \gamma)$ where $\mathbf{B}_0$ is the sharp interface Bond number and $b_{k,\gamma}$ is chosen so that the BHSCH linear growth rate matches that of the sharp interface for the most unstable wavenumber k in the initial data. Again, by Eq. (2.24), this amounts to taking gravity in the form $\tilde{G} = \tilde{G}_0(1 + g_{k,\gamma}\gamma)$. In the results up to now, we have taken $\mathbf{B} = \mathbf{B}_0$ and $\tilde{G} = \tilde{G}_0$.

Let us now reconsider the flow presented in section IV A ($|\mathbf{B}_0| = 25$). Here, we match the growth rates at $k = 1$. Recall from section 5.2 of Part I, $b_{1,.05} = 1.4148$ and $b_{1,.04} = 1.4025$. The evolution of the corresponding HSCH $c = 1/2$ contour lines is shown in figure 19; because of symmetry only approximately one half of the layer is displayed. The solid curve is the sharp interface result, the dashed and dashed-dot curves correspond to $\gamma = 0.04$ and 0.05 respectively. All other parameters are as in section IV A. There is now very good agreement between the models. Decreasing γ improves the agreement further. Up to $t = 7.0$, the largest differences occur on the sides of the rising bubbles where the HSCH curves have slightly steeper slopes. This causes the HSCH neck region to be slightly thicker than that of the sharp interface to conserve mass. At $t = 7.5$, we see that pinchoff has occurred in the HSCH case whereas in the sharp interface case, there is still a small distance between the upper and lower interfaces. This distance is on the order of the interface thickness, which is why there is pinchoff in the HSCH model.

To compare the performance of the HSCH and BHSCH results with the Bond numbers $\mathbf{B}$ and $\mathbf{B}_0$, we plot the interfaces at times $t = 7.0$ and 7.5 in figures 20(a) and (b) respectively with $\gamma = 0.04$. In these figures, the sharp interface (+) is plotted together with the $c = 1/2$ contours from the HSCH model, with $\mathbf{B}_0$ (dashed) and $\mathbf{B}$ (solid), and the BHSCH model with $\mathbf{B}_0$ (dotted) and $\mathbf{B}$ (dot-dashed). Note the dramatic improvement in the agreement between the HSCH/BHSCH and sharp interface models when the modified Bond number $\mathbf{B}$ is used. The differences observed between the HSCH and BHSCH results exhibit the features discussed as in section IV B.

Now we examine a flow with a more complicated initial condition containing several

wavenumbers. Let the initial interface positions be given by

$$y_2(x) = \pi + 0.5 + 0.025 \sum_{i=1}^{4} \cos(ix)$$
$$y_1(x) = \pi - 0.5 - 0.025 \sum_{i=1}^{4} \cos(ix),$$

which contains four Fourier modes. The initial condition $c(\mathbf{x}, 0)$ is then constructed via Eq. (4.2) with these values of y_1 and y_2. Again, we take $|\mathbf{B}_0| = 25$ and all other parameters (except $\mathbf{B}$) are as in section IV A. The most unstable mode is $k = 3$ (see section 5.2.2 in Part I). Therefore, we match the BHSCH and sharp interface growth rates at this wavenumber. Also from section 5.2.2 in Part I, we have $b_{3,.05} = 3.3782$ and $b_{3,.04} = 3.2101$. The HSCH $c = 1/2$ contour lines for the modified $\mathbf{B}$ are shown in figure 21. Again because of symmetry, only approximately one half of the layer is shown. The dashed and dot-dashed curves correspond to $\gamma = 0.04$ and 0.05 respectively and the sharp interface is the solid curve. The agreement between the models is quite good although the match is not as good as that in the previous case where the initial condition contains only the $k = 1$ wavenumber. Here we see the heights of the tallest fingers are slightly over-predicted while the heights of the lower fingers are slightly under-predicted. This is because we have matched only the $k = 3$ growth rate. For example, the tallest fingers correspond to the $k = 1$ mode which has a larger growth rate in the HSCH/BHSCH case than in the sharp interface case due to our choice of $\mathbf{B}$. Other more complicated modifications of the HSCH/BHSCH parameters, such as matching the growth rates of an unstable band of Fourier modes did not improve the agreement although our choices of HSCH parameters may not have been optimal. Again, pinchoff occurs in the HSCH case (before the sharp interface case) when the distance between the upper and lower sharp interfaces is on the order of the interface thickness.

We conclude this section with a flow using an even more complicated initial condition for which there is no apparent symmetry:

$$y_2(x) = \pi + 0.5 + 0.2 \sum_{i=1}^{5} \left[\cos(ix) - \cos((5+i)x) - \sin(2ix) \right],$$

$$y_1(x) = \pi - 0.5 - 0.2 \sum_{i=1}^{5} [\cos(ix) - \cos((5+i)x) - \sin(2ix)] \,,$$

which contains 10 Fourier modes. The initial concentration $c(\mathbf{x}, t)$ is constructed in the same manner as in the previous simulation. All the parameters are the same as in the previous simulation since $k = 3$ is still the most unstable wavenumber. The evolution of the sharp interface (solid) and the $\gamma = 0.04$ (dashed) and $\gamma = 0.05$ (dot-dashed) HSCH $c(\mathbf{x}, t) = 1/2$ contours is shown in figure 22. The agreement is quite good with $\gamma = 0.04$ contour being closer to the sharp interface. Although the initial condition is seen to be somewhat irregular, large scale fingers eventually dominate the flow and three large bubbles are produced by pinchoff. This is a reflection of $k = 3$ being the most unstable wavenumber. The bubbles tend to circularize due to surface tension as they rise.

F. Miscibility

As a final numerical investigation, let us suppose that the heavy and light components of the fluid are actually miscible, in contrast to the immiscible liquid/liquid flows we have considered up to this point. To model miscible case, one needs only to replace the non-convex free energy f_0 in the HSCH/BHSCH systems with a convex one. For simplicity, we take

$$f_0(c) = (c - 1/2)^2. \tag{4.7}$$

The flow geometry is as before (figure 1) and the other parameters are chosen as follows: $\gamma = 0.05$; $\mathbf{Pe} = 3/\gamma$; $\rho(c)$, τ, $\mathbf{C}$ and $\mathbf{M}$ are as in section IV A; $\mathbf{B} = -50$ for the upper interface ($\mathbf{B} = 50$ for the lower interface) and the viscosity $\eta(c) = (\eta_1 - \eta_2)c + \eta_2$ where η_1, η_2 are either 0.1 or 0.5 (i.e. $\mathbf{A} = \pm.667$). Note that the Bond number is really the initial Bond number since it is defined using the densities of the pure fluids. The density of the binary fluid $\rho(c)$, on the other hand, becomes uniform as the fluids mix.

The evolution of HSCH $c(\mathbf{x}, t)$ contours for these flows are graphed in figures 23 and 24. In figure 23, the higher viscosity fluid is the light fluid in interior of the layer. In this

case, the viscosity and gravitational instabilities are aligned. In figure 24, the viscosity of the heavy fluid is larger; here the viscosity and gravitational instabilities are misaligned. In the evolution process, the layer widens rapidly and the concentration becomes more uniform as the fluids mix. Observe that the concentration does not converge to $c = 1/2$, which is the well (minimum) of the free energy (4.7), as this would violate mass conservation. Instead, $c(\mathbf{x}, t)$ is converges to the value $\bar{c} = 0.14882$. Interestingly, when the light fluid is more viscous (Atwood number of upper interface is $\mathbf{A} = -.667$), the heavy less viscous fluid appears to finger through the light fluid eventually producing at time $t = 10$, "bubbles" of relatively light and heavy fluid components surrounded by fluid that has mixed more. In spirit, this is similar to the immiscible case. The bubbles decrease in size as the components mix. When the viscosities of the light and heavy fluids are reversed so that the heavy fluid is more viscous (Atwood number of upper interface is $\mathbf{A} = .667$), the tendency to finger is greatly reduced and the fluids mix diffusionally without much differential motion. The difference in behavior of the two flows may be explained by the fact that the former is more unstable since the less viscous fluid displaces the more viscous fluid. This enables the fingering instability to overcome the stabilizing effects of diffusion and dynamic surface tension.

Lastly, let us consider the dynamic or effective surface energy between the fluids. Since the fluids are miscible, there is no static surface tension. In the HSCH model, however, concentration gradients produce stresses which mimic those due to surface energy. Thus, one may measure the effective surface energy by measuring the gradients of concentration. Therefore, let us define

$$E_s(t) = \frac{\mathbf{C}}{2\mathbf{M}} \int |\nabla c|^2 \, dxdy$$

to be the dynamic surface energy. We note that in the simulations we presented previously where the fluids are immiscible, $E_s(t) = \tau \cdot (L_1(t) + L_2(t))/2 + O(\gamma)$ where τ is the sharp interface surface tension and $L_1(t)$, $L_2(t)$ are the lengths of the two interfaces. The matched asymptotic expansions in section 3.2 in Part I may be used to justify this statement. In

figure 25, we present $E_s(t)$ and its logarithm as functions of time for the simulation from figure 23. Observe that $E_s(t)$ decreases very rapidly at early times and eventually decays exponentially at later times which is consistent with the evolution of the c contours observed in figure 23. Thus, for this value of **Pe**, the diffusional forces are much stronger than the surface tension-like forces. The surface tension like forces play a role in the flow evolution only at very short times while at later times, the flow is influenced more by the competition between buoyancy, viscous and diffusional forces. We note that increasing the value of **Pe** decreases the strength of the diffusional forces.

V. CONCLUSIONS

In this paper, we have analyzed two physically-motivated model systems to study pinchoff and reconnection of a binary fluid in a Hele-Shaw cell. In one of the systems (HSCH), the binary fluid may be compressible due to diffusion. In the other system (BHSCH), a Boussinesq approximation is used and the binary fluid is incompressible. The miscibility of the fluid components is modelled by the free energy. If the components are miscible, the free energy is a convex function of concentration. If the components are immiscible, the free energy is non-convex. We primarily focused on the case of immiscible components.

We observed that the compressibility is important at topology transitions but not in the smooth regions of the flow. For example, $\nabla \cdot \mathbf{u}$ behaves like a delta function localized in space and time at pinchoff. This distinguishes the HSCH model from all others (including that of Folch et al. [59]) in which compressibility effects are neglected. It may turn out, for example, that characterizing the limiting effect of compressibility at pinchoff may suggest a physically-based selection mechanism for cutting and reconnecting sharp interfaces.

Furthermore, for smooth interfaces before pinchoff, we have demonstrated the convergence of the HSCH/BHSCH models to the classical sharp interface system by direct comparison of their respective fully nonlinear numerical solutions. For instance, over the (flow) time scales we consider, we do not observe artifacts such as the attraction of diffuse planar

interfaces [68] due to the long-range interaction of their exponential tails. The convergence we observe is linear in the parameter measuring the interface thickness. Following the linear stability analysis given in Part I, we have also shown that the HSCH/BHSCH parameters may be modified to achieve better agreement with the sharp interface results at a finite interface thickness. We improved the agreement between the models by simply modifying the Bond number by an amount approximately proportional to the interface thickness in order to match the sharp and BHSCH/HSCH growth rates at a particular unstable wavenumber. There may be other, more optimal choices of parameters.

We have also investigated the effects of Bond number and viscosity difference on the flows. We found that both influence the pinchoff time, the interface morphology and the number of satellite drops produced by pinchoff.

Lastly, we also considered a case in which the fluid components are miscible. We found competition between buoyancy, viscous and diffusional forces and at early times, surface tension-like forces. When the unstable stratification of density and viscosity are aligned, fingering is observed. Otherwise, diffusion seems to dominate and there is little differential motion of the fluids.

There are several directions in which this work will be taken in the future. First, we intend to pursue the development physically-based selection mechanisms for reconnecting sharp interfaces. This will require analyzing the detailed dynamics in the transition region and will require improved numerical methods that allow much smaller interface thicknesses to be resolved than in our current work. Through comparisons with experiments, the physical correctness of the model and selection mechanisms can be established. To this end, algorithms will be developed that use adaptive mesh refinement (AMR). See [69,70] for examples demonstrating the usefulness of adaptivity in the context of a finite element method for a phase field model. In our case, the primary difficulty will be to develop AMR for the fourth order nonlinear Cahn-Hilliard equation for concentration. While we anticipate AMR to be quite useful to reducing the allowable interface thickness, it is unlikely we will achieve resolutions which enable the interface thickness to be microscopic as may be the case in oil

and water mixtures. Nevertheless, our goal is to extrapolate our results to zero interface thickness and our work here suggests that this may be possible without microscopic interface thicknesses.

Second, we intend to compare our results with those obtained by other means such as the level set method and the volume of fluid method. We are interested in determining whether the methods agree post-pinchoff; before pinchoff agreement is to be expected. In the simpler context of interfacial motion by mean curvature, for example, the level set method and the zero thickness limit of the phase-field method both yield the unique viscosity solution [71,72]. However, since the above methods do not take compressibility into account, this effect at pinchoff may influence the results. In viscosity dominated flow regimes, such as in Hele-Shaw cells, small differences at pinchoff are likely damped out as suggested by our results in section IV B. When inertia becomes significant, small differences may be amplified leading to a wider range of observed behavior.

Third, we will bring the knowledge we have developed in the Hele-Shaw case to bear for simulations of the full equations (NSCH model) where inertia may be significant. We have already performed simulations of Boussinesq approximations of the NSCH equations in several flow regimes and geometries (see [40,41,73]) and found results consistent with those obtained here for the BHSCH model. For example, linear convergence to sharp interface models is observed and oppositely signed vorticity is created at pinchoff due to surface tension. In fact, experimental evidence for the production of this vorticity is given in [74–76]. However, it remains to take compressibility into account.

Fourth, and lastly, we will continue to pursue the use of the HSCH model (and also the NSCH model) for simulating multi-fluid flows with miscible components. We wish, for example, to compare with the experimental results (see e.g. [2]) as well as to results from other models of miscible fluids [62]. An appealing aspect of the miscible case is that since the fluids mix, the interface layer widens and becomes easier to resolve numerically.

ACKNOWLEDGMENTS

It is a pleasure to thank our colleagues B. Cockburn, G. Forest, P. Leo, E. Longmire, R. McLaughlin, Q. Nie, M. Shelley, L. Truskinovsky and M. Verschueren for helpful and interesting discussions concerning this work. The first two authors were partially supported by the Department of Energy (Office of Basic Sciences), the National Energy Research Computing Center (NERSC), the National Science Foundation and the Minnesota Supercomputer Institute. The second author thanks the Institute for Mathematics and its Applications for its hospitality.

REFERENCES

* Also in Department of Chemical Engineering and Materials Science, University of Minnesota; and in Department of Mathematics, University of North Carolina.

[1] H. Lee, J. Lowengrub and J. Goodman, submitted to Phys. Fluids.

[2] G.M. Homsy, Ann. Rev. Fluid Mech. **19**, 271 (1987).

[3] P.G. Saffman, J. Fluid Mech. **173**, 73 (1986).

[4] T. Hou, J. Lowengrub, and M. Shelley, Phys. Fluids **9**, 1933 (1997).

[5] P. Constantin, T.F. Dupont, R.E. Goldstein, L.P. Kadanoff, M.J. Shelley and S.-M. Zhou, Phys. Rev. E **47**, 4169 (1993).

[6] T.F. Dupont, R.E. Goldstein, L.P. Kadanoff and S.-M. Zhou, Phys. Rev. E **47**, 4182 (1993).

[7] R. Almgren, A. Bertozzi and M.P. Brenner, Phys. Fluids **8**, 1356 (1996).

[8] R. Goldstein, A. Pesci and M. Shelley, Phys. Rev. Lett. **70** 3665 (1993).

[9] R. Goldstein, A. Pesci and M. Shelley, Phys. Rev. Lett. **75**, 3665 (1995).

[10] R. Goldstein, A. Pesci and M. Shelley, Phys. Fluids **10**, 2701 (1998).

[11] R. Goldstein, A. Pesci and M. Shelley, Phys. Fluids to appear.

[12] T. Hou, J. Lowengrub, and M. Shelley, J. Comp. Phys. **114**, 312 (1994).

[13] T. Hou, J. Lowengrub, and M. Shelley, J. Comp. Phys. to appear.

[14] C.S. Peskin and D.M. McQueen, J. Comp. Phys. **25**, 220 (1977).

[15] J.M. Hyman, Physica D **12**, 396 (1984).

[16] S.O. Unverdi and G. Tryggvason, J. Comp. Phys. **100**, 25 (1992).

[17] H.S. Udaykumar, M.M. Rao and W. Shyy, Int. J. Numer. Methds. Fluids **22**, 691 (1996).

[18] N. Mansour and T. Lundgren, Phys. Fluids A **2**, 1141 (1990).

[19] M.R. Nobari, Y.-J. Jan and G. Tryggvason, Phys. Fluids **8**, 29 (1996).

[20] C.S. Peskin and B.F. Prince, J. Comp. Phys. **105**, 33 (1993).

[21] R. Cortez and M. Minion, J. Comp. Phys. **161**, 428 (2000).

[22] J. Eggers and T.F. Dupont, J. Fluid Mech. **262**, 205 (1994).

[23] J. Eggers, Phys. Fluids **7**, 941 (1995).

[24] J.B. Keller and M. Miksis, SIAM J. Appl. Math **43**, 268 (1983).

[25] J. Brackbill, D.B. Kothe and C. Zemach, J. Comp. Phys. **100**, 335 (1992).

[26] S. Osher and J. Sethian, J. Comp. Phys. **79**, 12 (1988).

[27] Y.C. Chang, T.Y. Hou, B. Merriman and S. Osher, J. Comp. Phys. **124**, 449 (1996).

[28] M. Sussman, P. Smereka and S. Osher, J. Comp. Phys. **114**, 146 (1994).

[29] M. Sussman and P. Smereka, J. Fluid Mech. **341**, 269 (1997).

[30] M. Sussman, A. Almgren, J. Bell, P. Collela, L. Howell and M. Welcome, J. Comp. Phys. **148**, 81 (1999).

[31] E.G. Puckett, A. Almgren, J. Bell, D. Marcus and W. Rider, J. Comp. Phys. **130**, 269 (1997).

[32] B. Lafaurie, C. Nardone, C. Scardoveli, S. Zaleski and G. Zanetti, J. Comp. Phys. **113**, 134 (1994).

[33] B. Nadiga and S. Zaleski, Eur. J. Mech. B/Fluids **15**, 885 (1996).

[34] R. Scardovelli and S. Zaleski, Ann. Rev. Fluid Mech. **31**, 567 (1999).

[35] D. Gueffier, J. Li, A. Nadim, R. Scardovelli and S. Zaleski, J. Comp. Phys. **152**, 423 (1999).

[36] R. Fedkiw, T. Aslam, B. Merriman and S. Osher, J. Comp. Phys. **152**, 457 (1999).

[37] T.Y. Hou, Z. Li, S. Osher and H. Zhao, J. Comp. Phys. **134**, 236 (1997).

[38] B.T. Helenbrook, L. Martinelli and C.K. Law, J. Comp. Phys. **148**, 366 (1999).

[39] J. Goodman, J. Lowengrub and M. Shelley, private communication.

[40] J. Lowengrub, J. Goodman, H. Lee, E. Longmire, M. Shelley and L. Truskinovsky, Chapman & Hall/CRC Res. Notes Math, **409** (1999).

[41] J. Goodman, J. Lowengrub, M. Shelley and L. Truskinovsky, in preparation.

[42] S.D. Poisson, Paris: Bachelier (1831).

[43] J.D. Van der Waals, Z. Phys. Chem. **13**, 657 (1894); english translation in J. Stat. Phys. **20**, 197 (1979).

[44] J.S. Rowlinson and B. Widom, *Molecular theory of capillarity*, Clarendon Press, Oxford (1979).

[45] H.T. Davis and L.E. Scriven, Adv. Chem. Phys. **49**, 357 (1982).

[46] D. Anderson, G.B. McFadden and A.A. Wheeler, Ann. Rev. Fluid Mech. **30**, 139 (1998).

[47] J. Lowengrub and L. Truskinovsky, R. Soc. Lond. Proc. Ser. A Math. Phys. Eng. Sci. **454**, 2617 (1998)

[48] J.W. Cahn and J.E. Hilliard, J. Chem. Phys. **28**, 688 (1958).

[49] W. E and P. Palffy-Muhoray, Phys. Rev. E **55**, R3844 (1997).

[50] F. Otto and W. E, J. Chem. Phys. **107**, 10177 (1997).

[51] A. Shinozaki and Y. Oono, Phys. Rev. A **45**, R2161 (1992).

[52] M. Verschueren, Ph.D. Thesis, Technische Universiteit Eindhoven, the Netherlands, 1999.

[53] H. Struchtrup and J.W. Dold, Interfaces and Free Boundaries, in review.

[54] M. Gurtin and G.B. McFadden, ed., I.M.A. Series in Mathematics and its Applications **43**, Springer, New York (1992).

[55] G. Caginalp, MA J. Appl. Math **44**, 77 (1990).

[56] G. Caginalp and X. Chen, Eur. J. Appl. Math **9**, 417 (1998).

[57] R.L. Pego, Proc. Roy. Soc. London Ser. A **422**, 261 (1989).

[58] N. Alikakos, P. Bates and X. Chen, Arch. Rat. Mech. Anal. **128**, 165 (1994).

[59] R. Folch, J. Casademunt, A. Hernandez-Machado and L. Ramirez-Piscina, Phys. Rev. E **60**, 1724 (1999); Phys. Rev. E **60**, 1734 (1999).

[60] P.G. Saffman and G.I. Taylor, Proc. Roy. Soc. London A **245**, 312 (1958).

[61] S. Allen and J.W. Cahn, Acta Metall. **27**, 1084 (1979).

[62] D.D. Joseph, Eur. J. Mech. Fluids **9**, 565 (1990).

[63] P.S. Perera and R.F. Sekerka, Phys. Fluids **9**, 376 (1997).

[64] C.-W. Park and G.M. Homsy, J. Fluid Mech **139**, 291 (1984).

[65] C. Canuto, M. Hussaini, A. Quarteroni, and T. Zang, *Spectral Methods in Fluid Dynamics*, Springer-Verlag, Berlin, 1988.

[66] P.H. Leo, J.S. Lowengrub and H.-J. Jou, Acta Materialia **46** 2113 (1998).

[67] P.H. Leo, J.S. Lowengrub and Q. Nie, J. Comp. Phys. **157** 44 (2000).

[68] X. Sun and M. Ward, Stud. Appl. Math. **105** 203 (2000).

[69] R. Nochetto, A. Schmidt and C. Verdi, I.M.A. Vol. Math. Appl. **113** 163 (1997).

[70] N. Provatas, N. Goldenfeld and J. Dantzig, J. Comp. Phys. **148** 265 (1999).

[71] L.C. Evans and J. Spruck, J. Diff. Geom. **33** 635 (1991).

[72] L.C. Evans, H.M. Soner and P.E. Souganidis, Comm. Pure Appl. Math. **45** 1097 (1992).

[73] J. Hageman, M.S. Thesis, Department of Aerospace and Mechanics, University of Minnesota, 1999.

[74] E.K. Longmire, D.L. Gefroh and J. Lowengrub, to appear in **Proceedings of the 1999 ASME/JSME Meeting**, San Francisco.

[75] D.L. Gefroh, B.S. honors thesis, Department of Aerospace Engineering and Mechanics, University of Minnesota, 1998.

[76] T.L. Norman, M.S. thesis, Department of Aerospace Engineering and Mechanics, University of Minnesota, 1999.

FIGURES

FIG. 1. Initial data for concentration (a) and its slice at $x = \pi$ (b) when $\gamma = 0.05$.

FIG. 2. Slice of the generalized chemical potential at $x = \pi$ obtained by using the orginal (dashed curve) and modified integrating factors (solid curve). $|B| = 25$, $\alpha = 0.1$ and $\gamma = 0.04$.

FIG. 3. Evolution of sharp interfaces using a boundary integral method with $|B| = 25$ and $\eta_1 = \eta_2$ at (a). $t = 0$; (b). $t = 4.0$; (c). $t = 6.0$; (d). $t = 7.5$.

FIG. 4. Contours of c for the HSCH model with $|B| = 25$, $\alpha = 0.1$ and $\gamma = 0.04$. (a). $t = 0$; (b). $t = 4.0$; (c). $t = 6.0$; (d). $t = 7.5$; (e). $t = 8.0$; (f). $t = 8.5$. The 0.1, 0.3, 0.5, 0.7 and 0.9 contours are shown.

FIG. 5. Contours of c for the BHSCH model with $|B| = 25$, $\alpha = 0.1$ and $\gamma = 0.04$. (a). $t = 0$; (b). $t = 4.0$; (c). $t = 6.0$; (d). $t = 7.5$; (e). $t = 8.0$; (f). $t = 8.5$. The 0.1, 0.3, 0.5, 0.7 and 0.9 contours are shown.

FIG. 6. Vorticity and Concentration contours for HSCH model from figure 4. Dotted curve: $c = 1/2$ contour, solid curves: postive vorticity $\omega = (0.25, 0.75) \cdot \omega_{max}$, dashed curves: negative vorticity $\omega = (0.25, 0.75) \cdot \omega_{min}$. (a). $t = 7.0$; (b). $t = 7.5$; (c). $t = 8.0$; (d). $t = 8.5$; (e). $t = 8.5$ close-up of satellite drop region.

FIG. 7. Evolution of the maximum of vorticity for the HSCH result from figure 4 for different values of γ. (a). Maximum vorticity $\|\omega_(\cdot, t)\|_\infty$ with $\gamma = 0.04$ (solid), $\gamma = 0.05$ (dashed), $\gamma = 0.06$ (dot-dashed) and $\gamma = 0.08$ (dotted); (b). Scaled maximum: $\gamma\|\omega_(\cdot, t)\|_\infty$; (c). maximum of vorticity (solid) and the maximum of vorticity due to surface tension ('o').

FIG. 8. Contours of c at time $t = 8.5$ for the HSCH result from figure 4 for different values of γ. (a). $\gamma = 0.08$; (b). $\gamma = 0.06$; (c). $\gamma = 0.05$; (d). $\gamma = 0.04$.

FIG. 9. Convergence of HSCH result from figure 4 to sharp interface. (a). $c = 0.5$ contours for the HSCH r esult at time $t = 7.5$ (before pinchoff) from figure 4 for different values of γ– $\gamma = 0.04$ (dashed), $\gamma = 0.05$ (dot-dashed), $\gamma = 0.06$ (dotted), sharp interface ($\gamma = 0$, solid); (b). Convergence of the y-intercept of the upper $c = 0.5$ contour to the sharp interface; (c). $c = 0.5$ contours for the HSCH result at time $t = 8.0$ (after pinchoff) from figure 4 for different values of γ; (d). Convergence of the y-intercept of the upper $c = 0.5$ contour.

FIG. 10. Comparison of HSCH and BHSCH results near pinchoff from figures 4 and 5 with $\gamma = 0.04$. The solid/dashed curves are the $c = 0.5$ contour lines of the HSCH/BHSCH results respectively. The vectors are the difference in velocities: $\mathbf{u}_{HSCH} - \mathbf{u}_{BHSCH}$. (a). $t = 7.5$; (b). $t = 7.6$; (c). $t = 7.65$; (d). $t = 7.7$.

FIG. 11. The contours of $\nabla \cdot \mathbf{u}$ at time $t = 7.6$ for the HSCH result from figure 4 with $\gamma = 0.04$. The $c = 0.5$ contour is the dotted curve. The solid curves are the $(0.25, 0.5, 0.75) \cdot \max(\nabla \cdot \mathbf{u})$ contours (positive values). The dashed curves are the $(0.25, 0.5, 0.75) \cdot \min(\nabla \cdot \mathbf{u})$ contours (negative values).

FIG. 12. Slices of various quantities for the HSCH result from figure 4 at time $t = 7.7$. The slices are taken at the value of x for which the $\max(\nabla \cdot \mathbf{u})$ is attained. (a). Slice of c; (b). Slice of components of μ: $f_0'(c)$ ($= \mu_0(c)$, solid), $-\mathbf{C}\Delta c$ (dashed), $\alpha \mathbf{M} q$ (dot-dashed); (c) Slice of μ; (d). Slice of $\nabla \cdot \mathbf{u}$.

FIG. 13. Evolution of $\nabla \cdot \mathbf{u}$ near pinchoff of HSCH result from figure 4 for different values of γ. $\gamma = 0.04$ ('o'), $\gamma = 0.05$ ('square'), $\gamma = 0.06$ ('diamond'). (a). $\min(\nabla \cdot \mathbf{u})$; (b). $\max(\nabla \cdot \mathbf{u})$.

FIG. 14. The limit of $\nabla \cdot \mathbf{u}$ as $\gamma \to 0$. Slices of $\nabla \cdot \mathbf{u}$ at $x = x_*$, where the minumum of $\nabla \cdot \mathbf{u}$ is achieved, for the HSCH result from figure 11 for different values of γ. (a). $\gamma = 0.06$; (b). $\gamma = 0.05$; (c). $\gamma = 0.04$.

FIG. 15. The effect of density variation. The $c = 0.5$ contours for the HSCH model using $\gamma = 0.05$ and $\alpha = 0.05$ (solid) and $\alpha = 0.2$ (dashed). All other parameters are as in figure 11. (a). $t = 7.0$; (b). $t = 7.5$; (c). $t = 7.55$; (d) $t = 7.6$; (e). $t = 7.7$; (f). $t = 8.0$.

FIG. 16. The effect of Bond number. The $c = 0.5$ contours for the HSCH model with $\alpha = 0.1$, $\gamma = 0.04$. Leftmost column: $|\mathbf{B}| = 35$; Center column: $|\mathbf{B}| = 25$; Rightmost column: $|\mathbf{B}| = 35$.

FIG. 17. The effect of Bond number on the maximum vorticity in the HSCH model. Parameters as in figure 16. Solid curve: $|\mathbf{B}| = 15$; Dashed curve: $|\mathbf{B}| = 25$; Dot-dashed curve: $|\mathbf{B}| = 15$.

FIG. 18. The effect of viscosity difference on the $c = 0.5$ contours in the HSCH model. $\gamma = 0.05$, $\alpha = 0.1$ and $|\mathbf{B}| = 25$. Leftmost column: $\eta_1 = \eta_2 = 0.5$; Center column: $\eta_1 = 0.125$, $\eta_2 = 0.5$; Rightmost column $\eta_1 = 0.5$, $\eta_2 = 0.125$.

FIG. 19. The effect of modifying the Bond number to match the $k = 1$ sharp interface growth rate. $\alpha = 0.1$ and the $c = 0.5$ contour lines from the HSCH model are shown with $\gamma = 0.04$ (dashed, $|\mathbf{B}| = 25(1 + 1.4025\gamma)$) and $\gamma = 0.05$ (dot-dashed, $|\mathbf{B}| = 25(1 + 1.4148\gamma)$) together with the sharp interface (solid, $|\mathbf{B}| = 25$). Due to symmetry, approximately one half of the layer is shown. (a). $t = 0$; (b). $t = 2.0$; (c). $t = 4.0$; (d). $t = 6.0$; (e). $t = 7.0$; (f). $t = 7.5$.

FIG. 20. Close-up of comparison of modified Bond number HSCH $c = 0.5$ contours with the sharp interface result. $\gamma = 0.04$ and $\alpha = 0.1$. Sharp interface (+ curves); HSCH and BHSCH models with $\mathbf{B}| = 25$ (dashed and dotted curves respectively); HSCH and BHSCH models with $|\mathbf{B}| = 25(1 + 1.4025\gamma)$ (solid and dot-dashed curves respectively). (a). $t = 7.0$; (b). $t = 7.5$.

FIG. 21. The effect of modifying the Bond number to match the $k = 3$ sharp interface growth rate. $\alpha = 0.1$ and the $c = 0.5$ contour lines from the HSCH model are shown with $\gamma = 0.04$ (dashed, $|\mathbf{B}| = 25(1 + 3.2101\gamma)$) and $\gamma = 0.05$ (dot-dashed, $|\mathbf{B}| = 25(1 + 3.3782\gamma)$) together with the sharp interface (solid, $|\mathbf{B}| = 25$). Due to symmetry, approximately one half of the layer is shown. (a). $t = 0$; (b). $t = 1.0$; (c). $t = 2.0$; (d). $t = 3.0$; (e). $t = 4.0$; (f). $t = 4.5$.

FIG. 22. The effect of modifying the Bond number to match the $k = 3$ sharp interface growth rate with a more complicated, 10 mode initial condition. $\alpha = 0.1$ and the $c = 0.5$ contour lines from the HSCH model are shown with $\gamma = 0.04$ (dashed, $|\mathbf{B}| = 25(1 + 3.2101\gamma)$) and $\gamma = 0.05$ (dot-dashed, $|\mathbf{B}| = 25(1 + 3.3782\gamma)$) together with the sharp interface (solid, $|\mathbf{B}| = 25$). (a). $t = 0$; (b). $t = 2.0$; (c). $t = 4.0$; (d). $t = 4.5$; (e). $t = 5.0$; (f). $t = 6.0$.

FIG. 23. The effect of miscibility. The contour lines of c are shown from the HSCH model with $|\mathbf{B}| = 50$, $\gamma = 0.05$, $\alpha = 0.1$, $\mathbf{Pe} = 3/\gamma$, $\eta_1 = 0.5$ and $\eta_2 = 0.1$. (a). $t = 0$; (b). $t = 2.0$; (c). $t = 4.0$; (d). $t = 6.0$; (e). $t = 8.0$; (f). $t = 10.0$.

FIG. 24. The effect of miscibility. The contour lines of c are shown from the HSCH model with $|\mathbf{B}| = 50$, $\gamma = 0.05$, $\alpha = 0.1$, $\mathbf{Pe} = 3/\gamma$, $\eta_1 = 0.1$ and $\eta_2 = 0.5$. (a). $t = 0$; (b). $t = 2.0$; (c). $t = 4.0$; (d). $t = 6.0$; (e). $t = 8.0$; (f). $t = 10.0$.

FIG. 25. The evolution of surface energy in the miscible case from figure 23. (a). The surface energy $E_s(t)$; (b). The $\log(E_s(t))$.

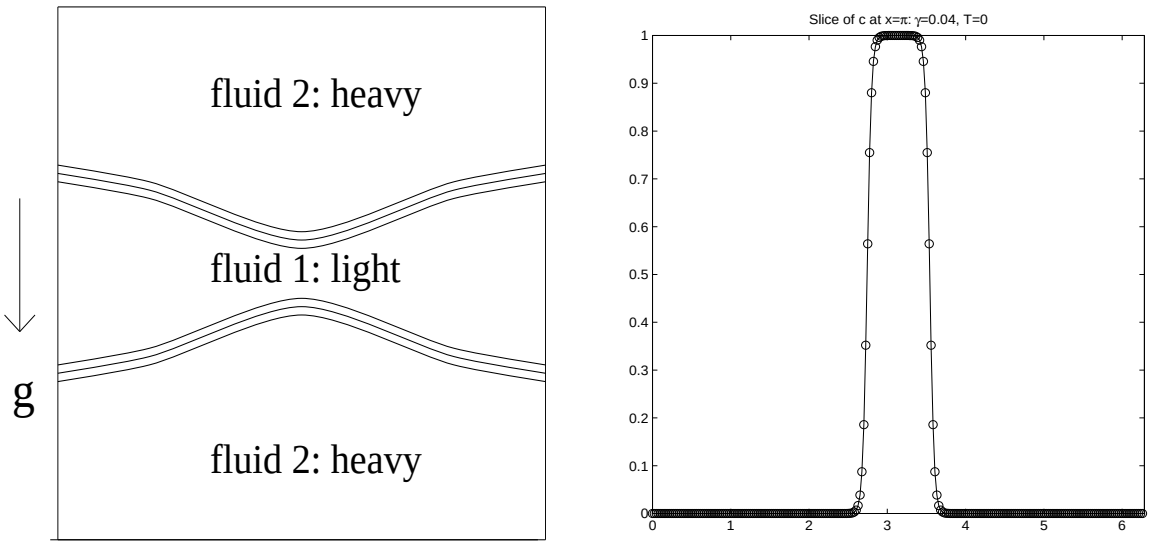

FIG. 1. Lee et al., Phys. Fluids, Initial data for concentration (a) and its slice at $x = \pi$ (b) when $\gamma = 0.04$.

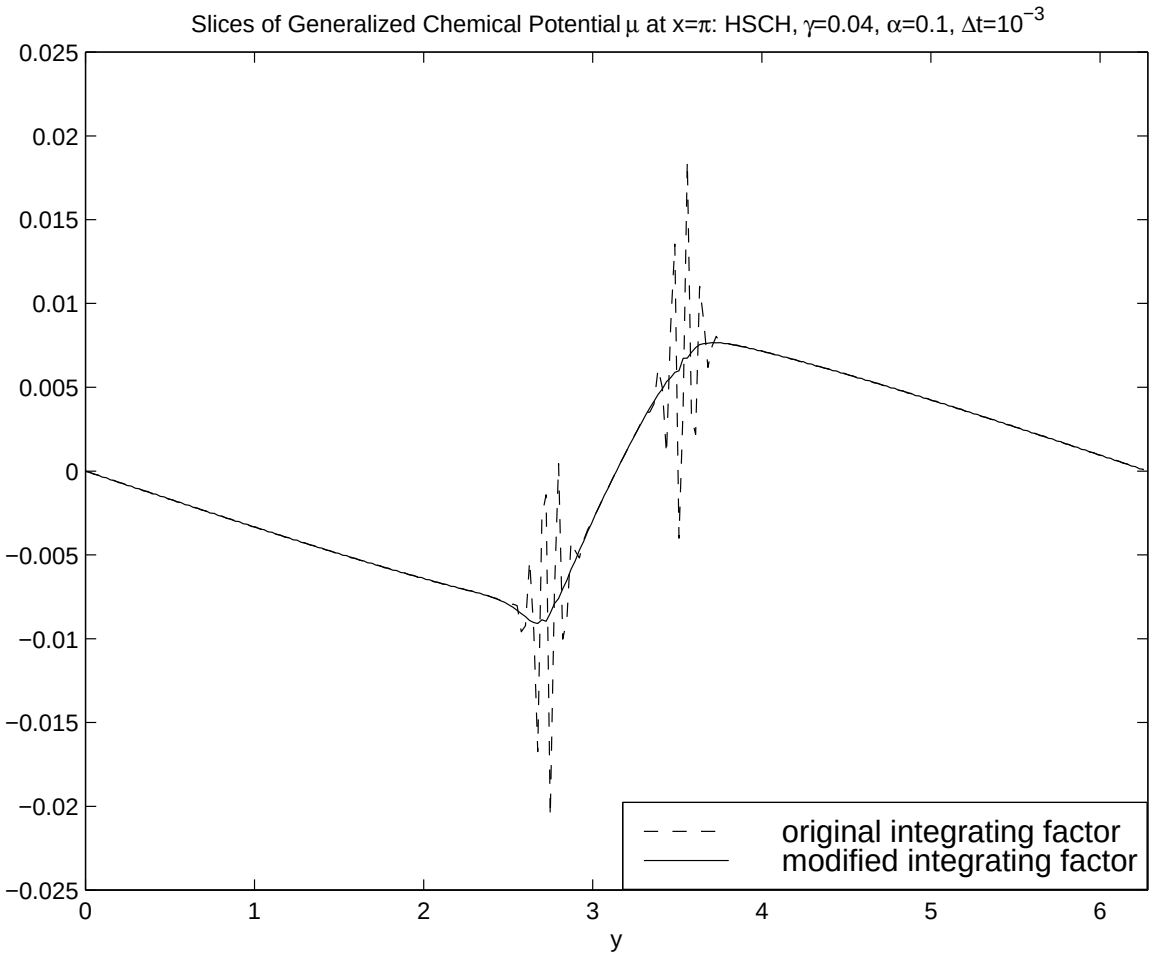

FIG. 2. Lee et al., Phys. Fluids, Slice of the generalized chemical potential at $x = \pi$ obtained by using the orginal (dashed curve) and modified integrating factors (solid curve). $|B| = 25$, $\alpha = 0.1$ and $\gamma = 0.04$.

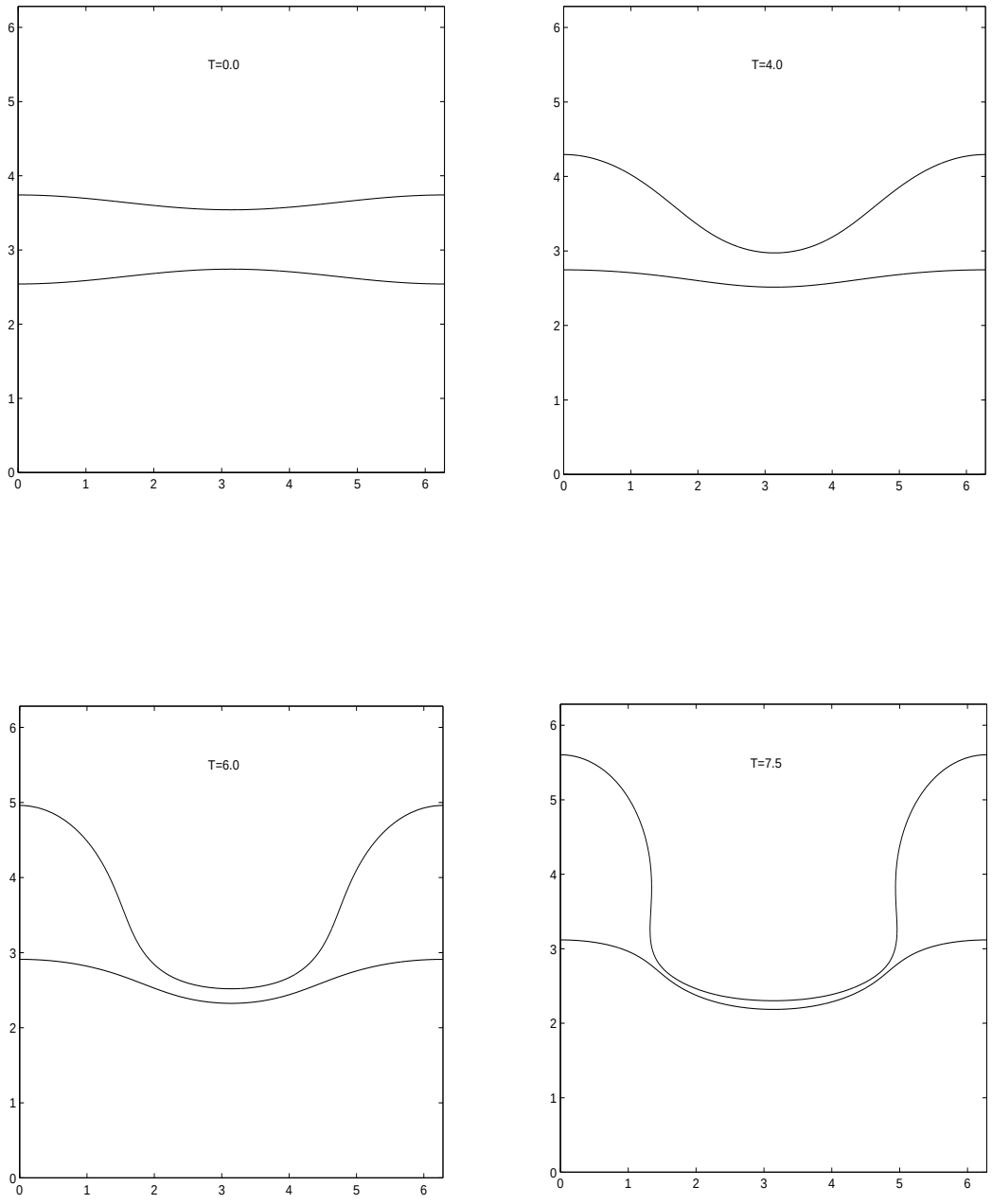

FIG. 3. Lee et al., Phys. Fluids, Evolution of sharp interfaces using a boundary integral method with $|B| = 25$ and $\eta_1 = \eta_2$ at (a). $t = 0$; (b). $t = 4.0$; (c). $t = 6.0$; (d). $t = 7.5$.

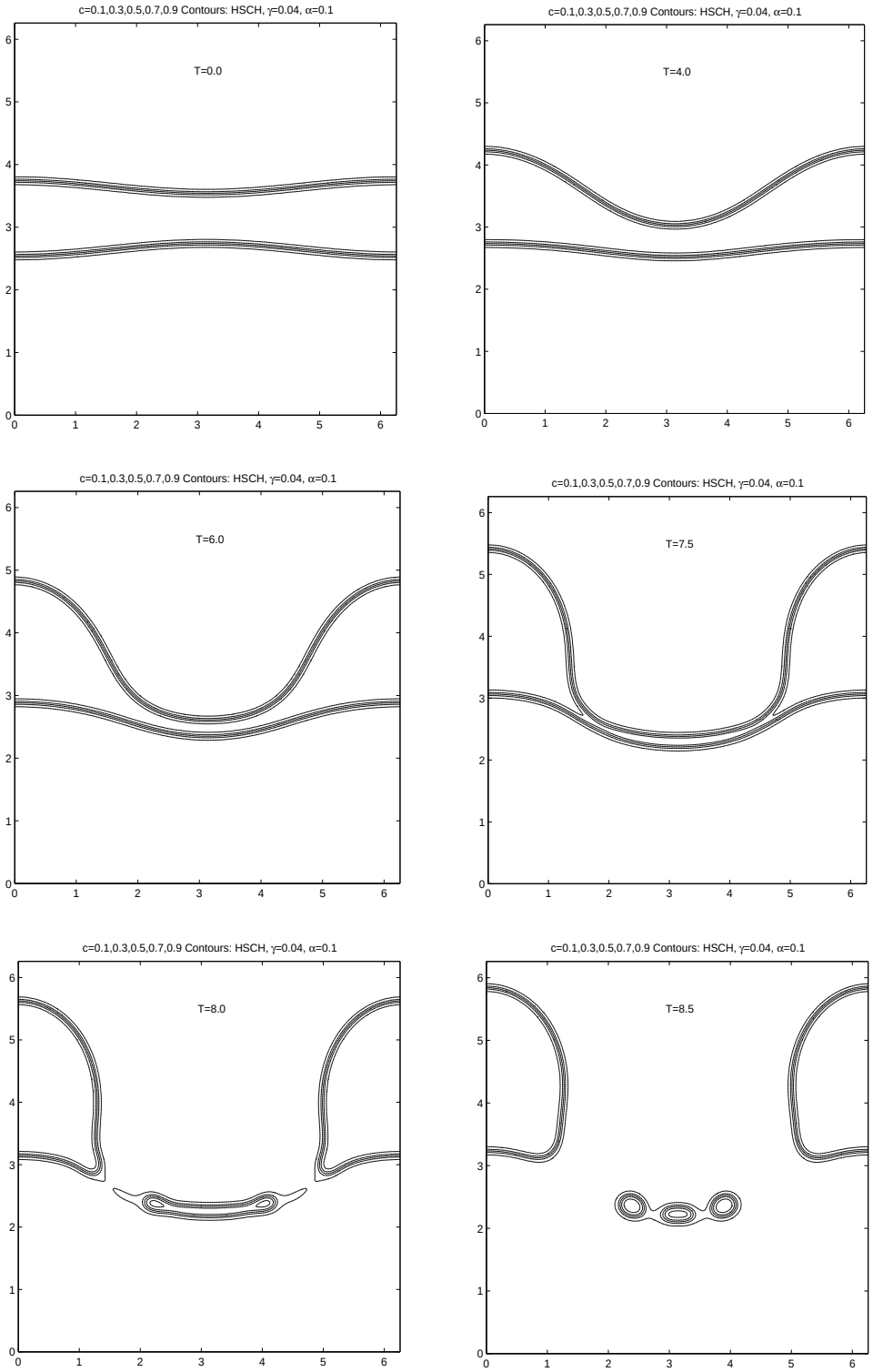

FIG. 4. Lee et al., Phys. Fluids, Contours of c for the HSCH model with $|B| = 25$, $\alpha = 0.1$ and $\gamma = 0.04$. (a). $t = 0$; (b). $t = 4.0$; (c). $t = 6.0$; (d). $t = 7.5$; (e). $t = 8.0$; (f). $t = 8.5$. The 0.1, 0.3, 0.5, 0.7 and 0.9 contours are shown.

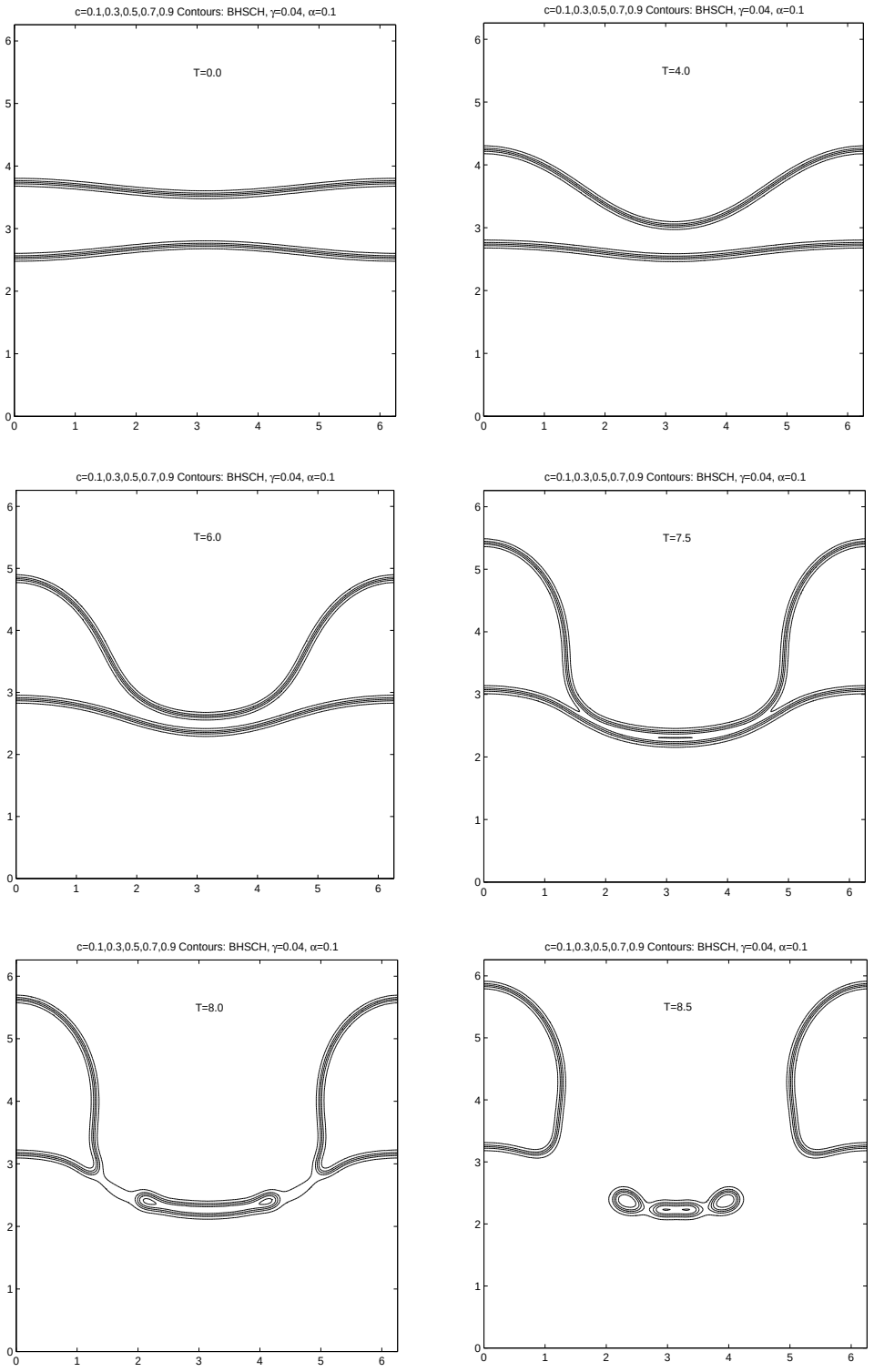

FIG. 5. Lee et al., Phys. Fluids, Contours of c for the BHSCH model with $|B| = 25$, $\alpha = 0.1$ and $\gamma = 0.04$. (a). $t = 0$; (b). $t = 4.0$; (c). $t = 6.0$; (d). $t = 7.5$; (e). $t = 8.0$; (f). $t = 8.5$. The 0.1, 0.3, 0.5, 0.7 and 0.9 contours are shown.

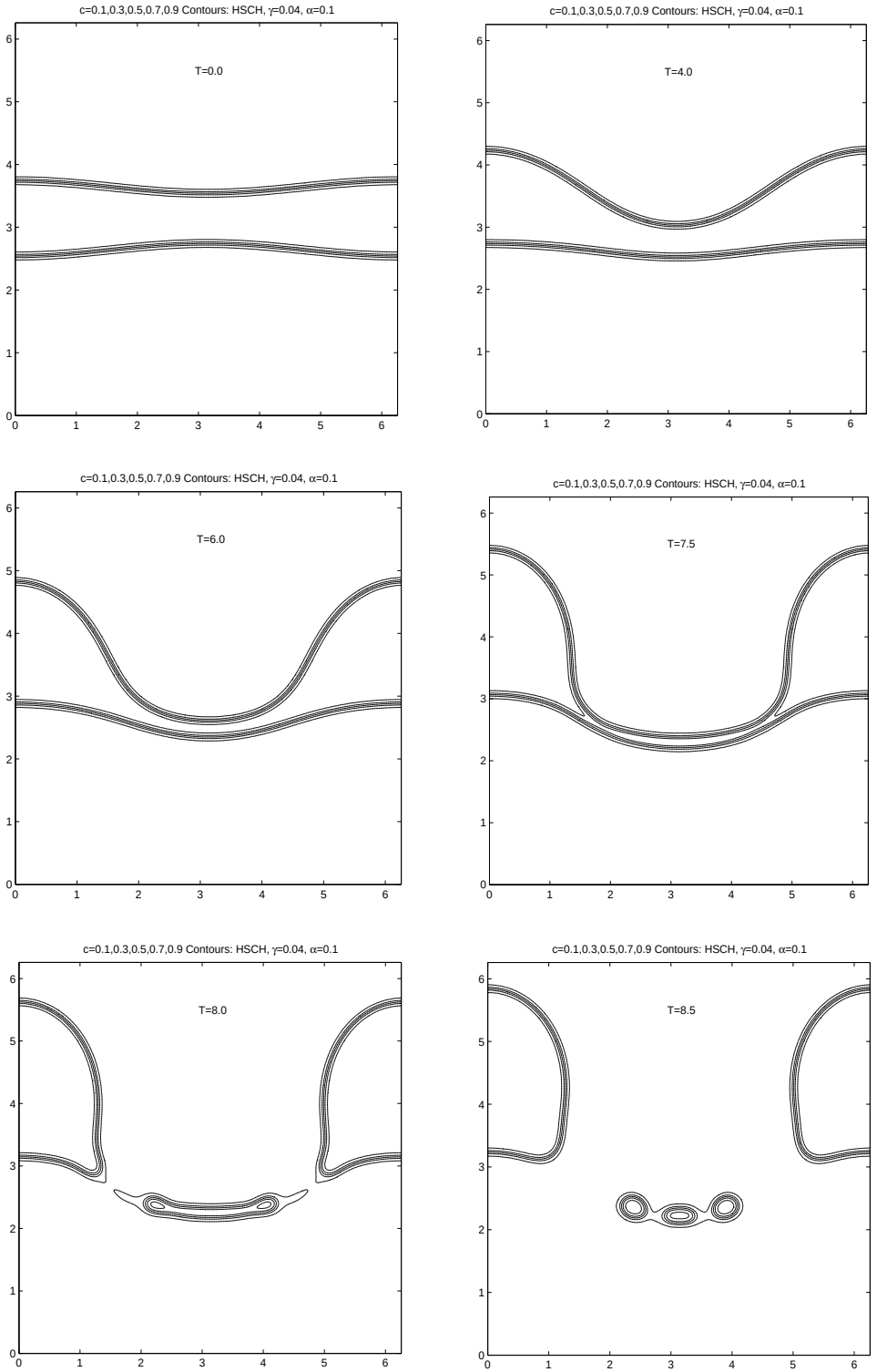

FIG. 6. Lee et al., Phys. Fluids, Vorticity and Concentration contours for HSCH model from figure 4. Dotted curve: $c = 1/2$ contour, solid curves: postive vorticity $\omega = (0.25, 0.75) \cdot \omega_{max}$, dashed curves: negative vorticity $\omega = (0.25, 0.75) \cdot \omega_{min}$. (a). $t = 7.0$; (b). $t = 7.5$; (c). $t = 8.0$; (d). $t = 8.5$; (e). $t = 8.5$ close-up of satellite drop region.

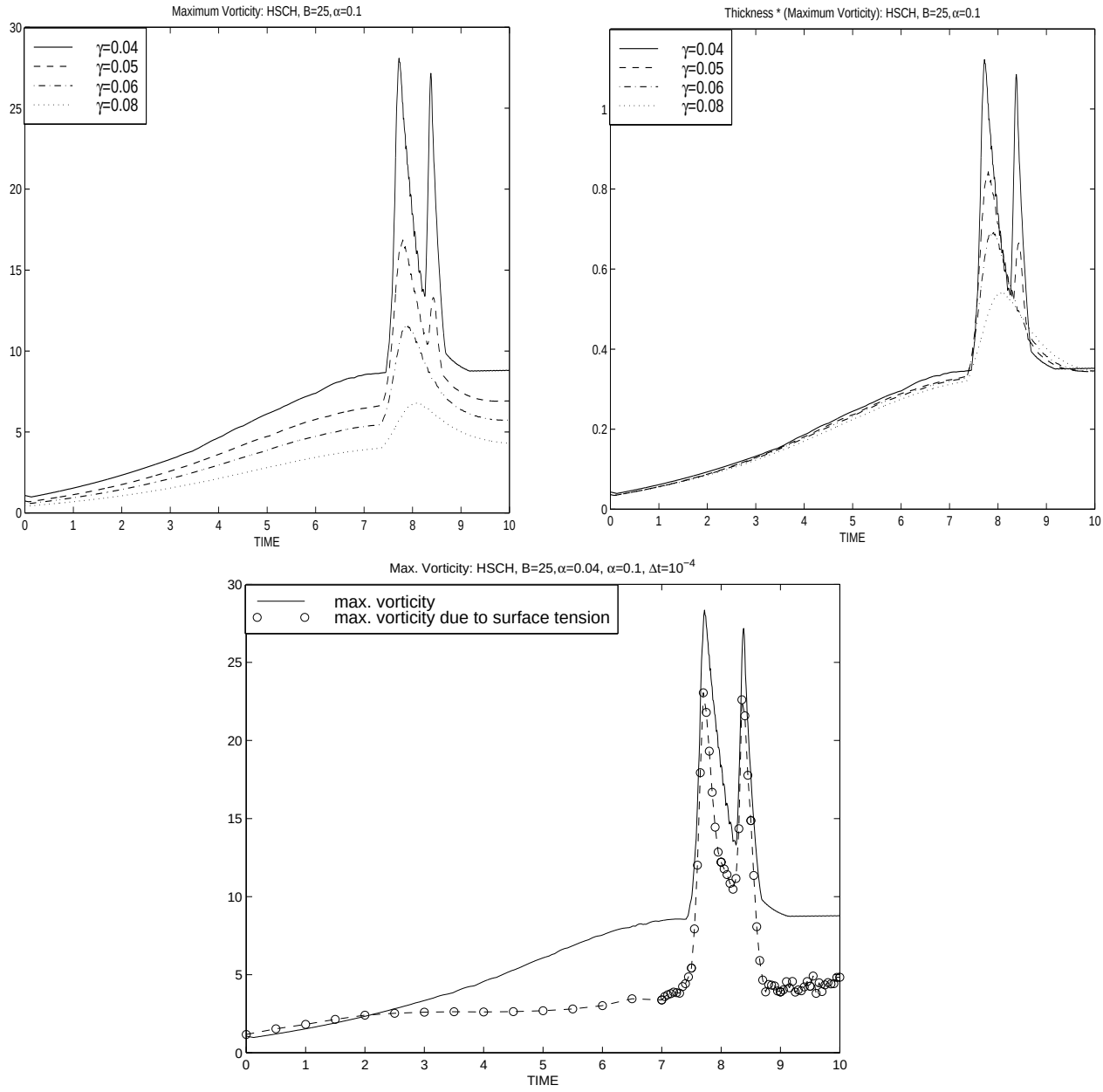

FIG. 7. Lee et al., Phys. Fluids, Evolution of the maximum of vorticity for the HSCH result from figure 4 for different values of γ. (a). Maximum vorticity $\|\omega_(\cdot,t)\|_\infty$ with $\gamma = 0.04$ (solid), $\gamma = 0.05$ (dashed), $\gamma = 0.06$ (dot-dashed) and $\gamma = 0.08$ (dotted); (b). Scaled maximum: $\gamma\|\omega_(\cdot,t)\|_\infty$; (c). maximum of vorticity (solid) and the maximum of vorticity due to surface tension ('o').

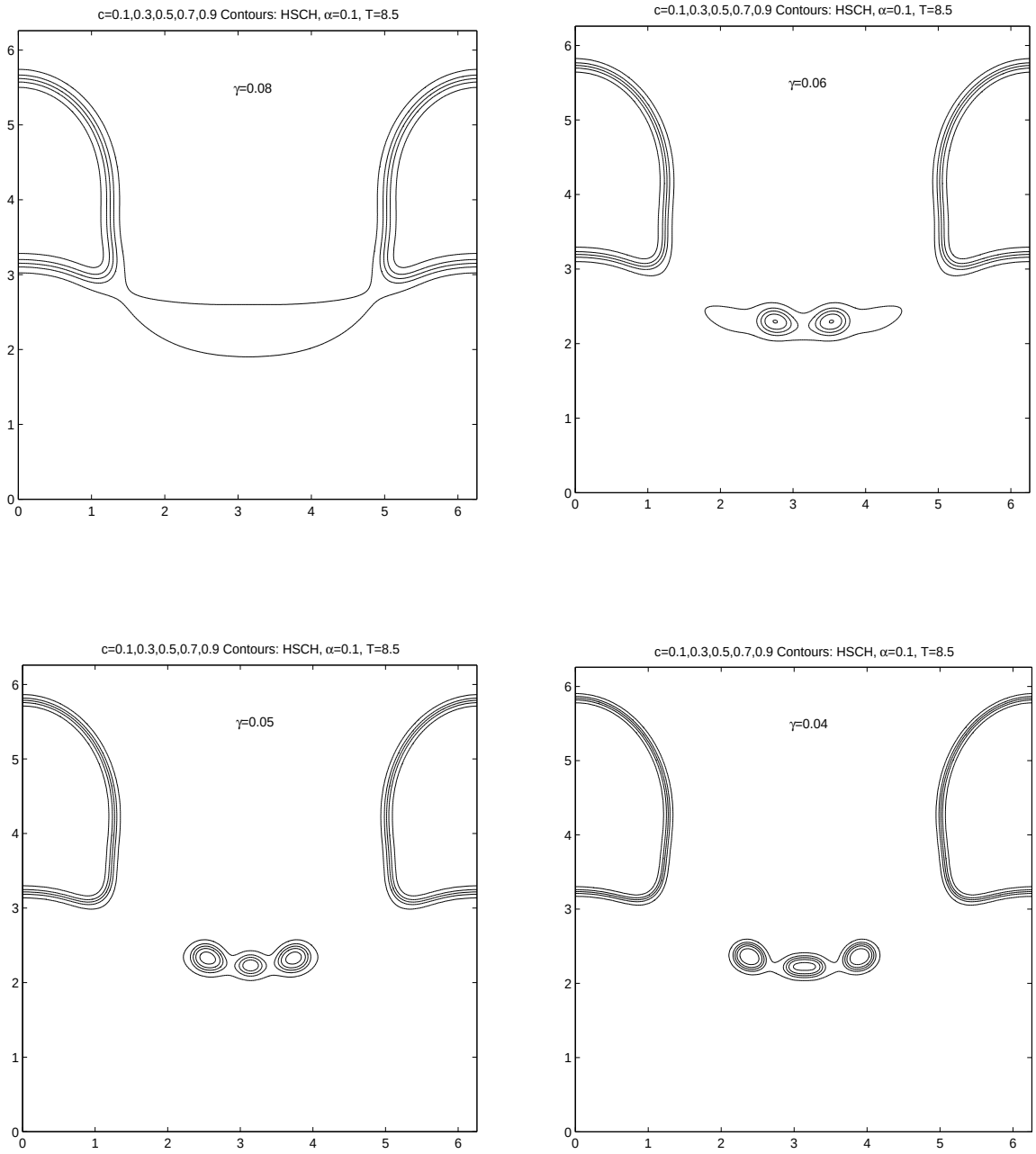

FIG. 8. Lee et al., Phys. Fluids, Contours of c at time $t = 8.5$ for the HSCH result from figure 4 for different values of γ. (a). $\gamma = 0.08$; (b). $\gamma = 0.06$; (c). $\gamma = 0.05$; (d). $\gamma = 0.04$.

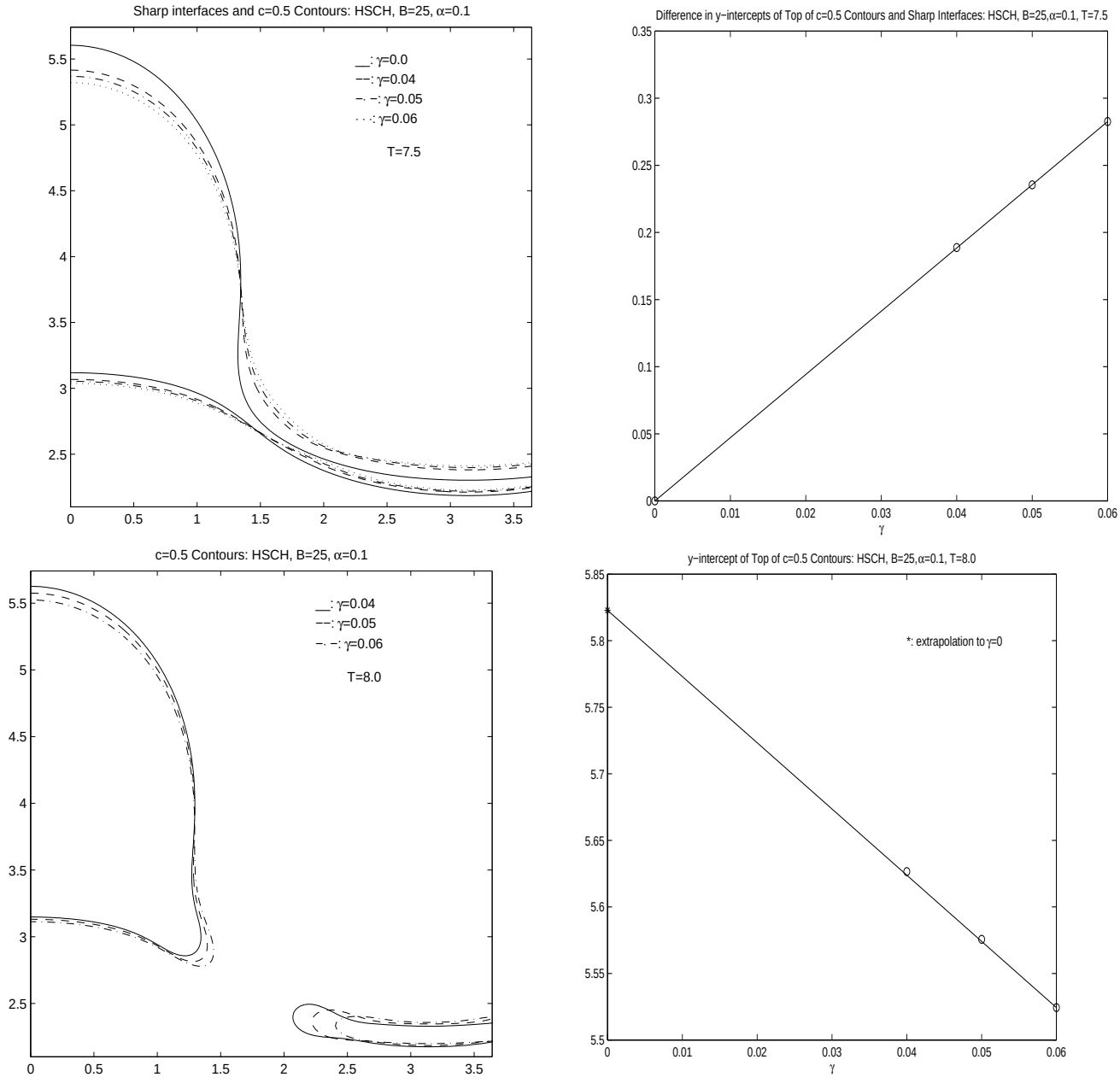

FIG. 9. Lee et al., Phys. Fluids, Convergence of HSCH result from figure 4 to sharp interface. (a). $c = 0.5$ contours for the HSCH r esult at time $t = 7.5$ (before pinchoff) from figure 4 for different values of γ– $\gamma = 0.04$ (dashed), $\gamma = 0.05$ (dot-dashed), $\gamma = 0.06$ (dotted), sharp interface ($\gamma = 0$, solid); (b). Convergence of the y-intercept of the upper $c = 0.5$ contour to the sharp interface; (c). $c = 0.5$ contours for the HSCH result at time $t = 8.0$ (after pinchoff) from figure 4 for different values of γ; (d). Convergence of the y-intercept of the upper $c = 0.5$ contour.

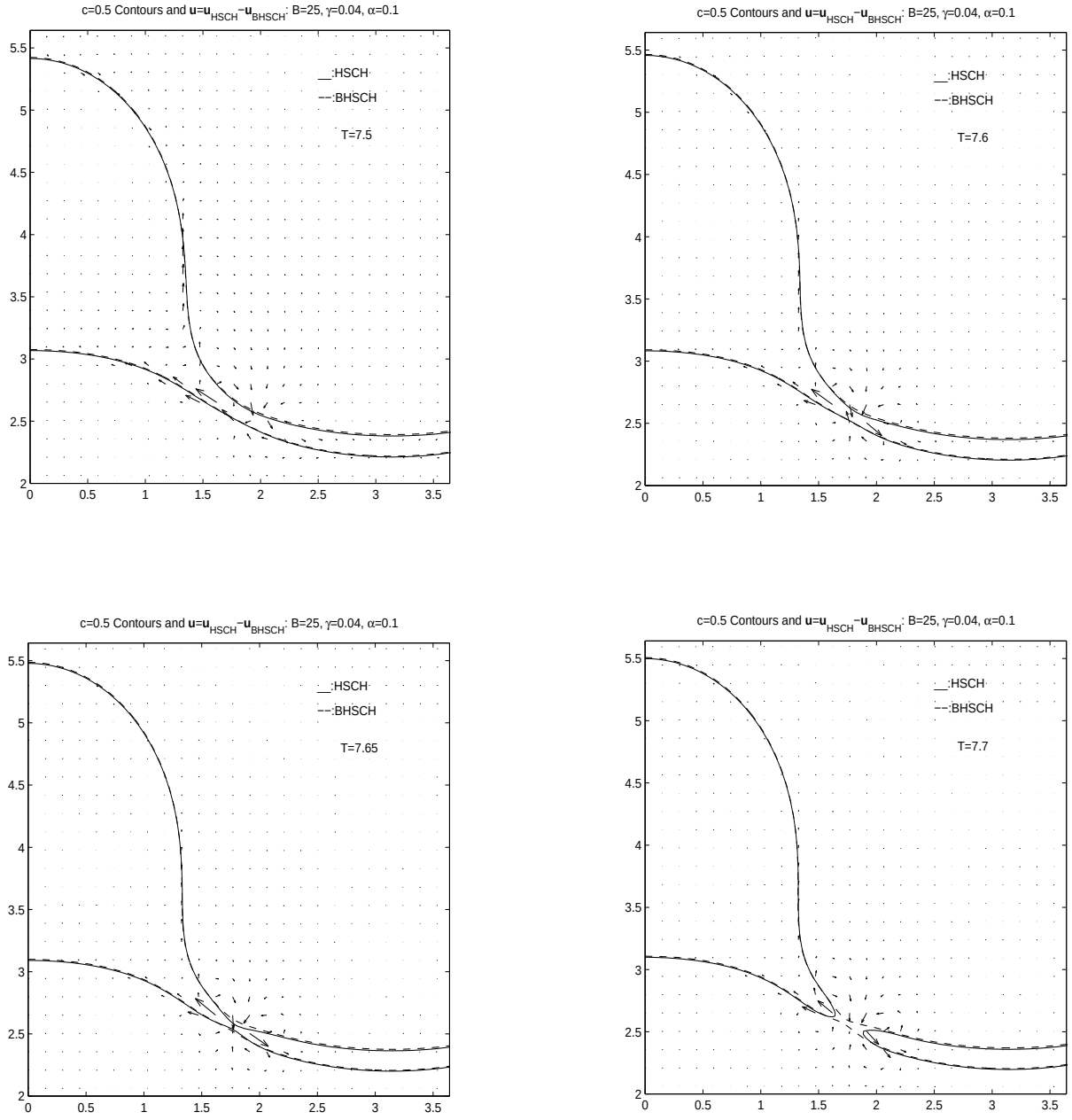

FIG. 10. Lee et al., Phys. Fluids, Comparison of HSCH and BHSCH results near pinchoff from figures 4 and 5 with $\gamma = 0.04$. The solid/dashed curves are the $c = 0.5$ contour lines of the HSCH/BHSCH results respectively. The vectors are the difference in velocities: $\mathbf{u}_{HSCH} - \mathbf{u}_{BHSCH}$. (a). $t = 7.5$; (b). $t = 7.6$; (c). $t = 7.65$; (d). $t = 7.7$.

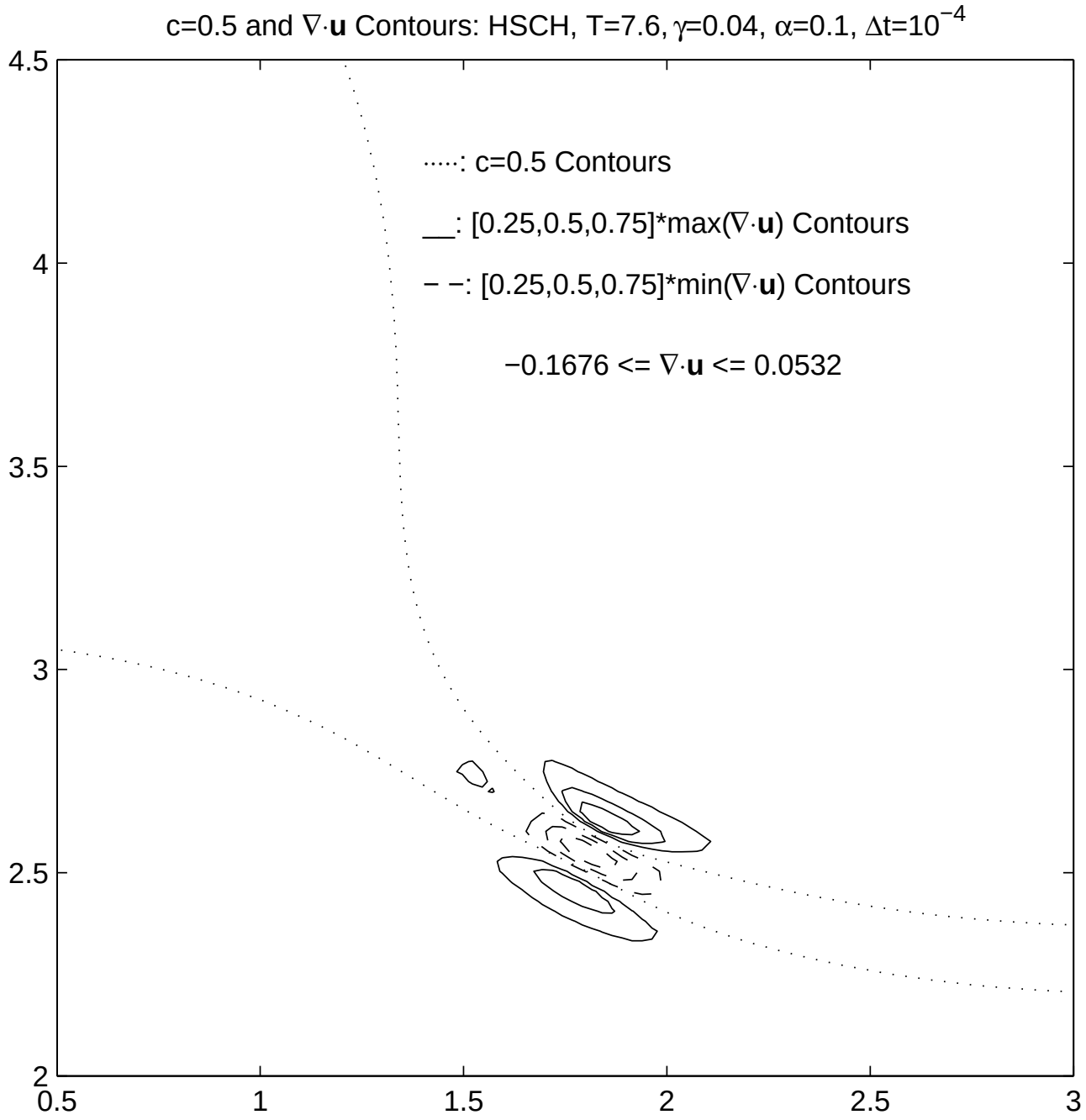

FIG. 11. Lee et al., Phys. Fluids, The contours of $\nabla \cdot \mathbf{u}$ at time $t = 7.6$ for the HSCH result from figure 4 with $\gamma = 0.04$. The $c = 0.5$ contour is the dotted curve. The solid curves are the $(0.25, 0.5, 0.75) \cdot \max(\nabla \cdot \mathbf{u})$ contours (positive values). The dashed curves are the $(0.25, 0.5, 0.75) \cdot \min(\nabla \cdot \mathbf{u})$ contours (negative values).

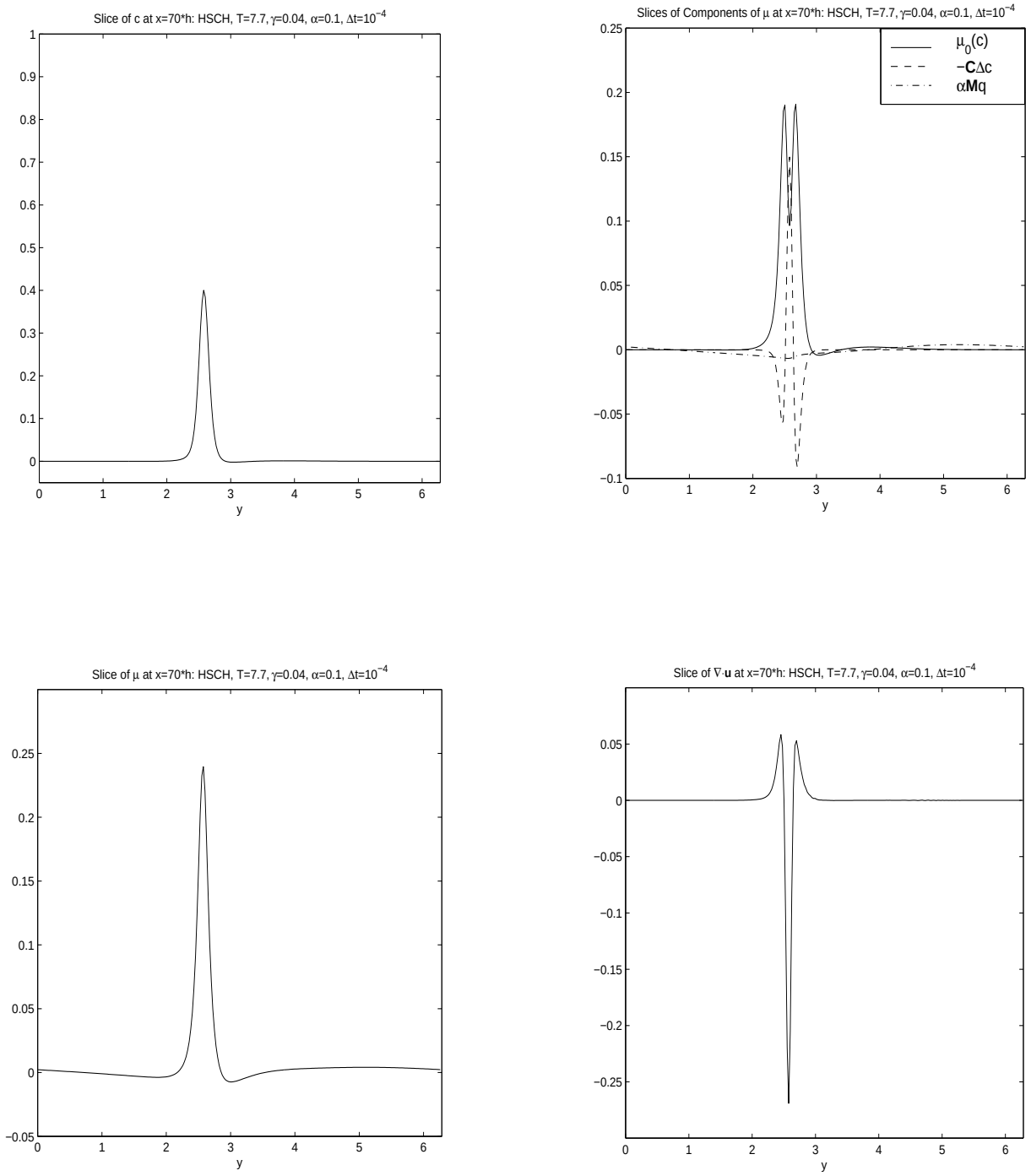

FIG. 12. Lee et al., Phys. Fluids, Slices of various quantities for the HSCH result from figure 4 at time $t = 7.7$. The slices are taken at the value of x for which the $\max(\nabla \cdot \mathbf{u})$ is attained. (a). Slice of c; (b). Slice of components of μ: $f_0'(c)$ $(= \mu_0(c)$, solid), $-\mathbf{C}\Delta c$ (dashed), $\alpha \mathbf{M} q$ (dot-dashed); (c) Slice of μ; (d). Slice of $\nabla \cdot \mathbf{u}$.

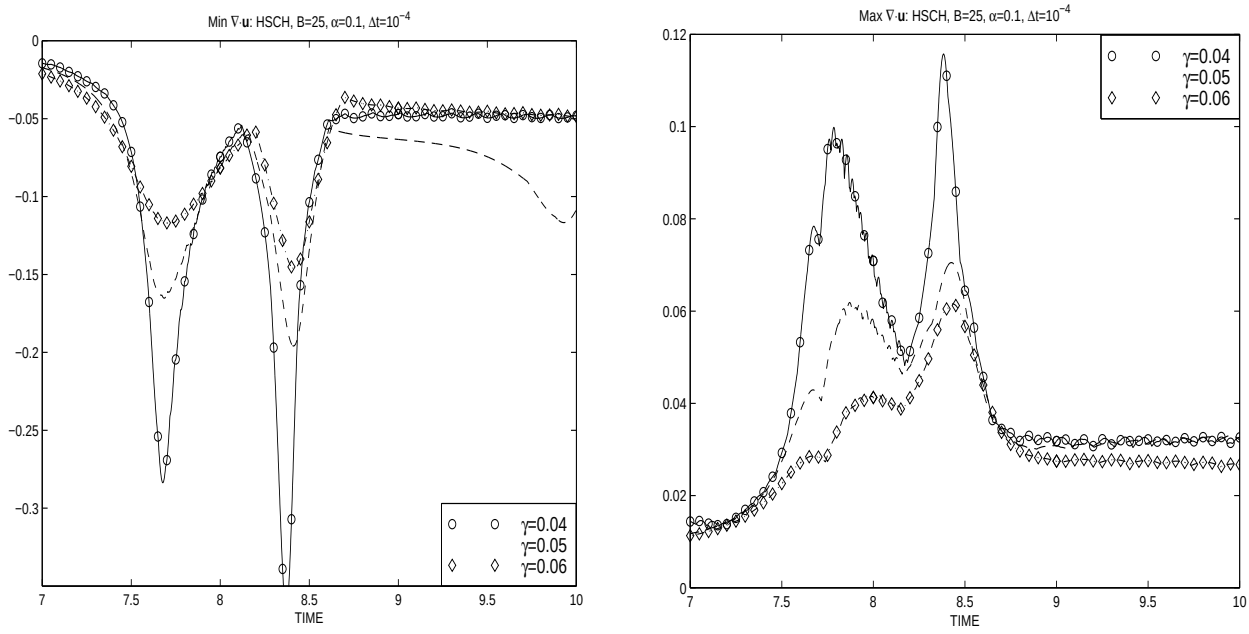

FIG. 13. Lee et al., Phys. Fluids, Evolution of $\nabla \cdot \mathbf{u}$ near pinchoff of HSCH result from figure 4 for different values of γ. $\gamma = 0.04$ ('o'), $\gamma = 0.05$ ('square'), $\gamma = 0.06$ ('diamond'). (a). $\min(\nabla \cdot \mathbf{u})$; (b). $\max(\nabla \cdot \mathbf{u})$.

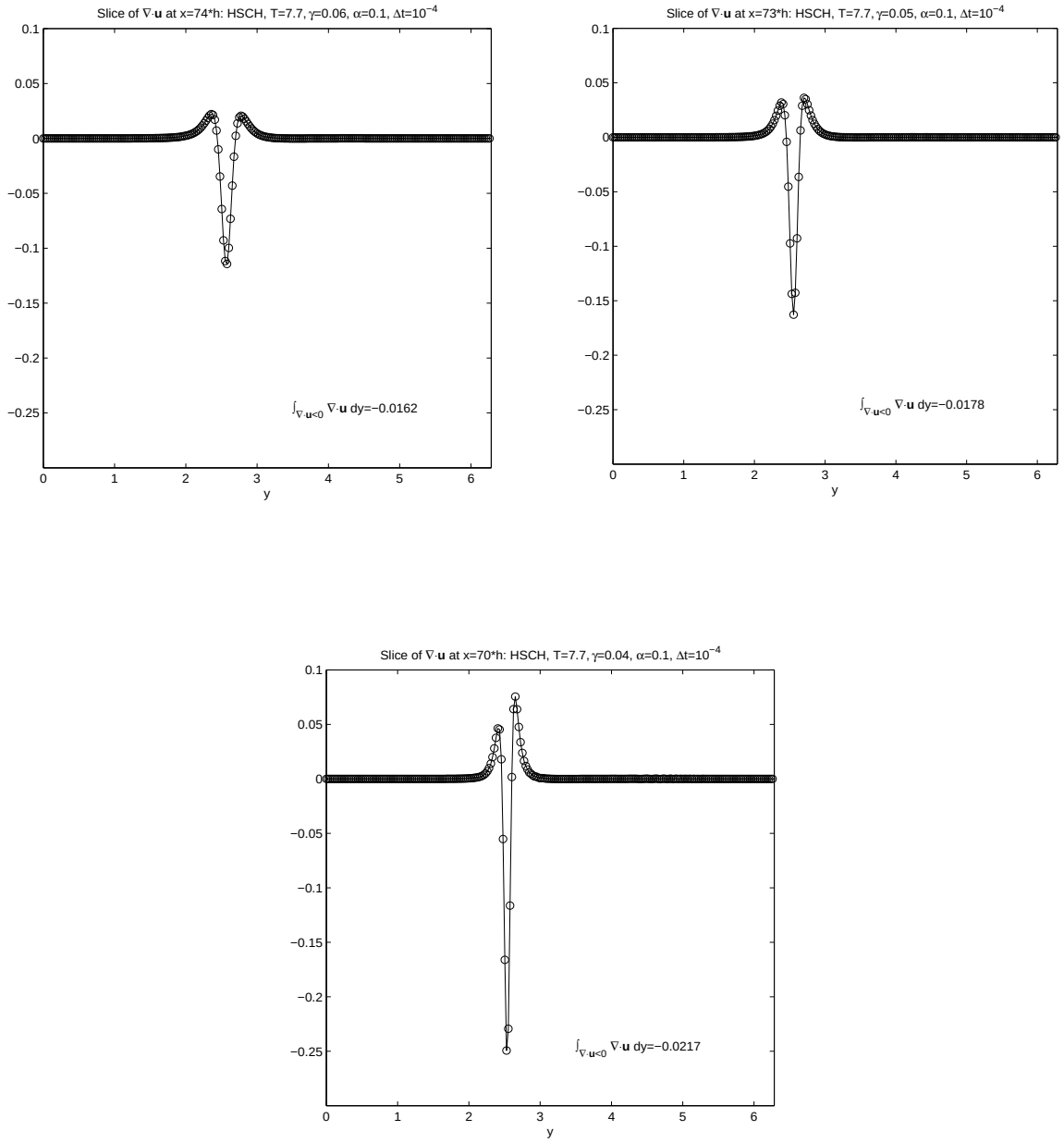

FIG. 14. Lee et al., Phys. Fluids, The limit of $\nabla \cdot \mathbf{u}$ as $\gamma \to 0$. Slices of $\nabla \cdot \mathbf{u}$ at $x = x_*$, where the minumum of $\nabla \cdot \mathbf{u}$ is achieved, for the HSCH result from figure 11 for different values of γ. (a). $\gamma = 0.06$; (b). $\gamma = 0.05$; (c). $\gamma = 0.04$.

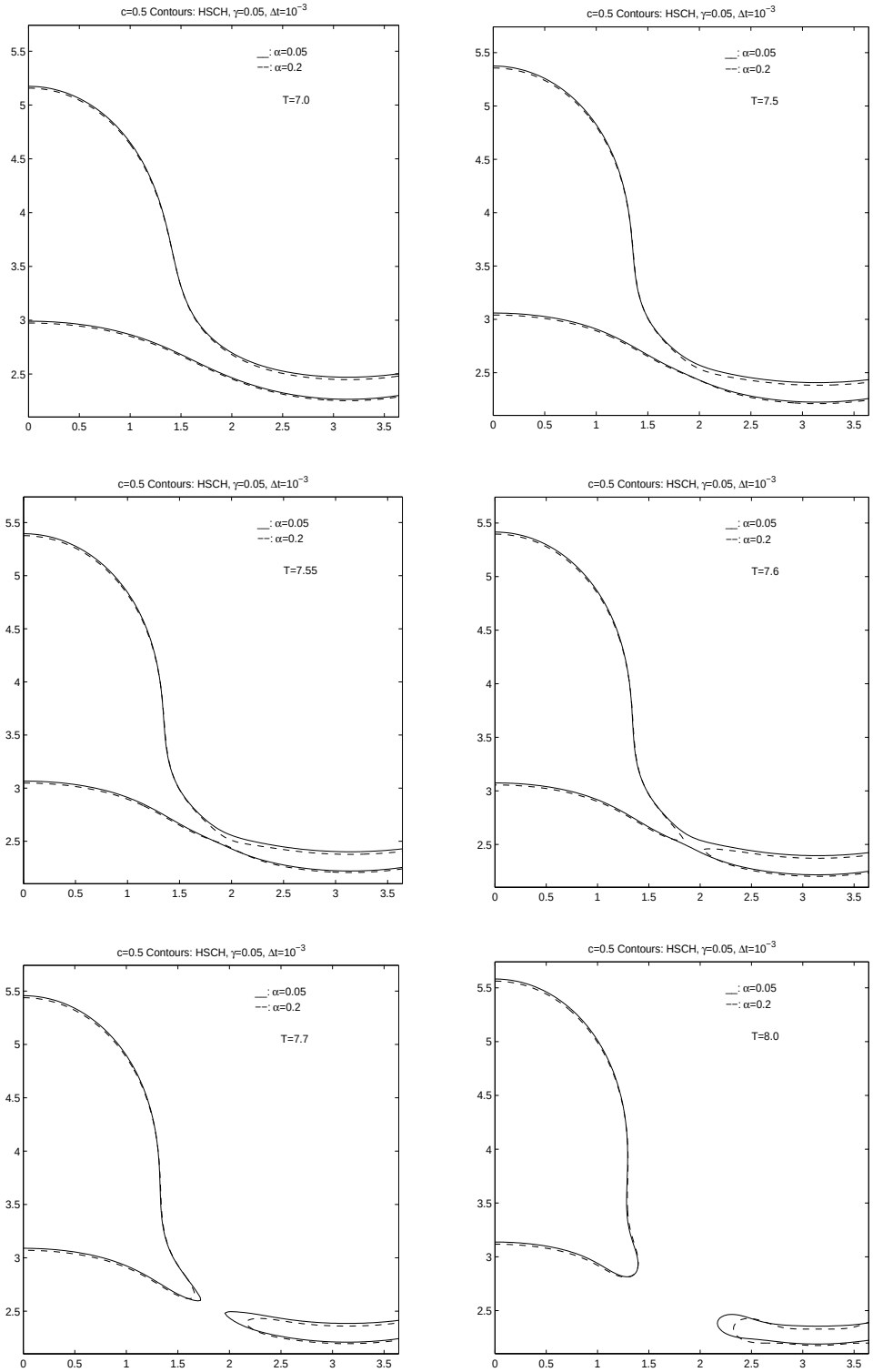

FIG. 15. Lee et al., Phys. Fluids, The effect of density variation. The $c = 0.5$ contours for the HSCH model using $\gamma = 0.05$ and $\alpha = 0.05$ (solid) and $\alpha = 0.2$ (dashed). All other parameters are as in figure 11. (a). $t = 7.0$; (b). $t = 7.5$; (c). $t = 7.55$; (d) $t = 7.6$; (e). $t = 7.7$; (f). $t = 8.0$.

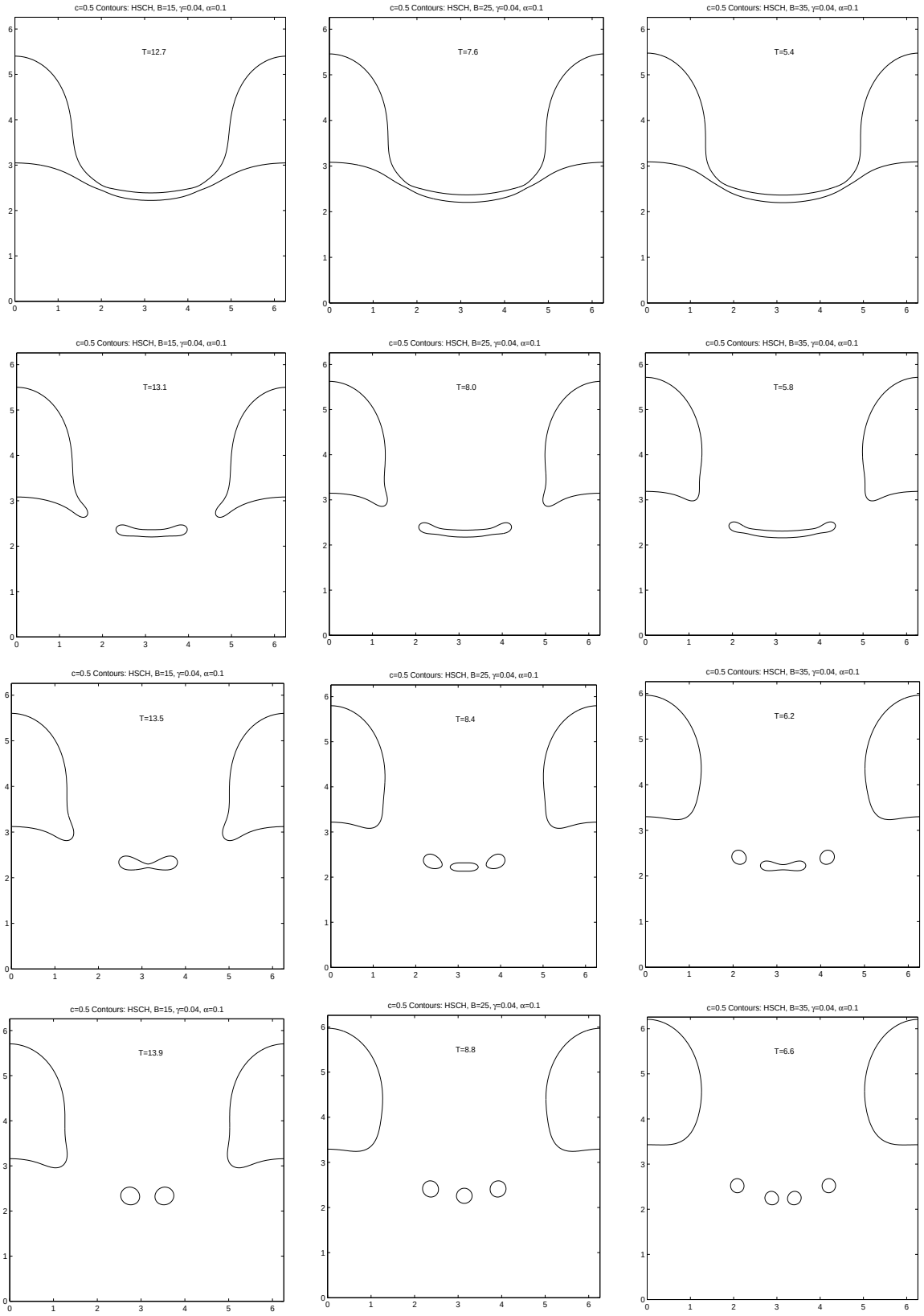

FIG. 16. Lee et al., Phys. Fluids, The effect of Bond number. The $c = 0.5$ contours for the HSCH model with $\alpha = 0.1$, $\gamma = 0.04$. Leftmost column: $|\mathbf{B}| = 15$; Center column: $|\mathbf{B}| = 25$; Rightmost column: $|\mathbf{B}| = 35$.

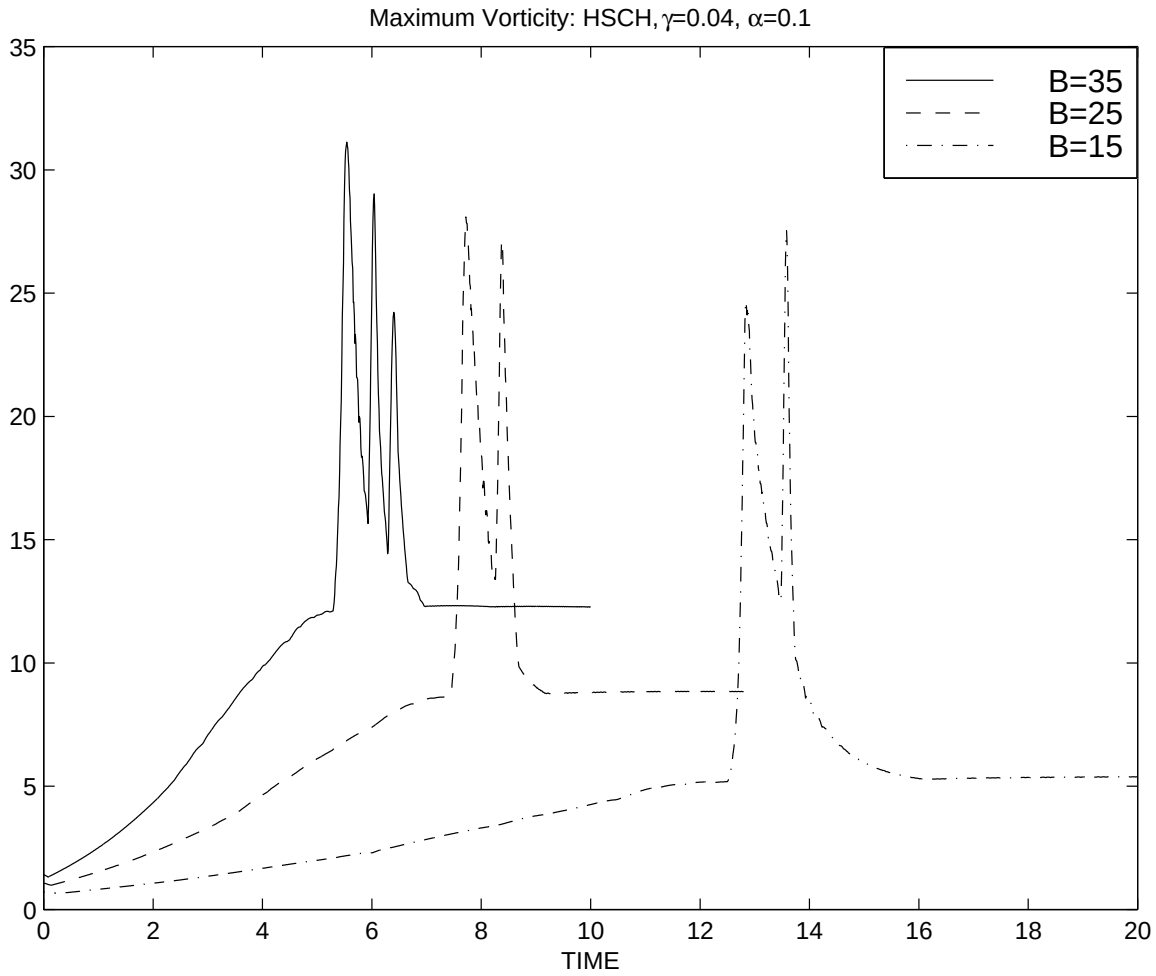

FIG. 17. Lee et al., Phys. Fluids, The effect of Bond number on the maximum vorticity in the HSCH model. Parameters as in figure 11. Solid curve: $|\mathbf{B}| = 35$; Dashed curve: $|\mathbf{B}| = 25$; Dot-dashed curve: $|\mathbf{B}| = 15$.

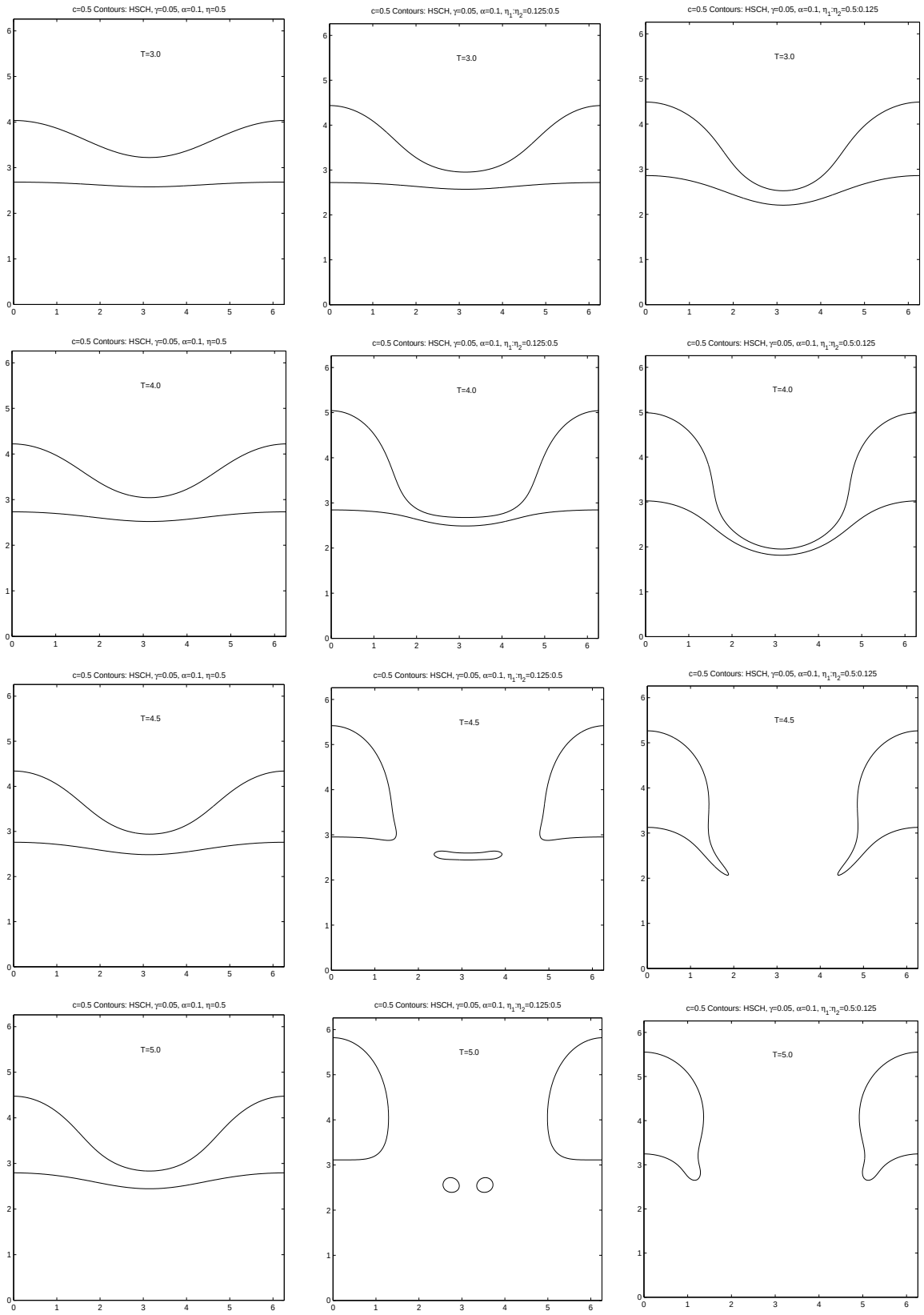

FIG. 18. Lee et al., Phys. Fluids, The effect of viscosity difference on the $c = 0.5$ contours in the HSCH model. $\gamma = 0.05$, $\alpha = 0.1$ and $|\mathbf{B}| = 25$. Leftmost column: $\eta_1 = \eta_2 = 0.5$ ($\mathbf{A} = 0$); Center column: $\eta_1 = 0.125$, $\eta_2 = 0.5$ ($\mathbf{A} = 0.6$); Rightmost column $\eta_1 = 0.5$, $\eta_2 = 0.125$ ($\mathbf{A} = -0.6$).

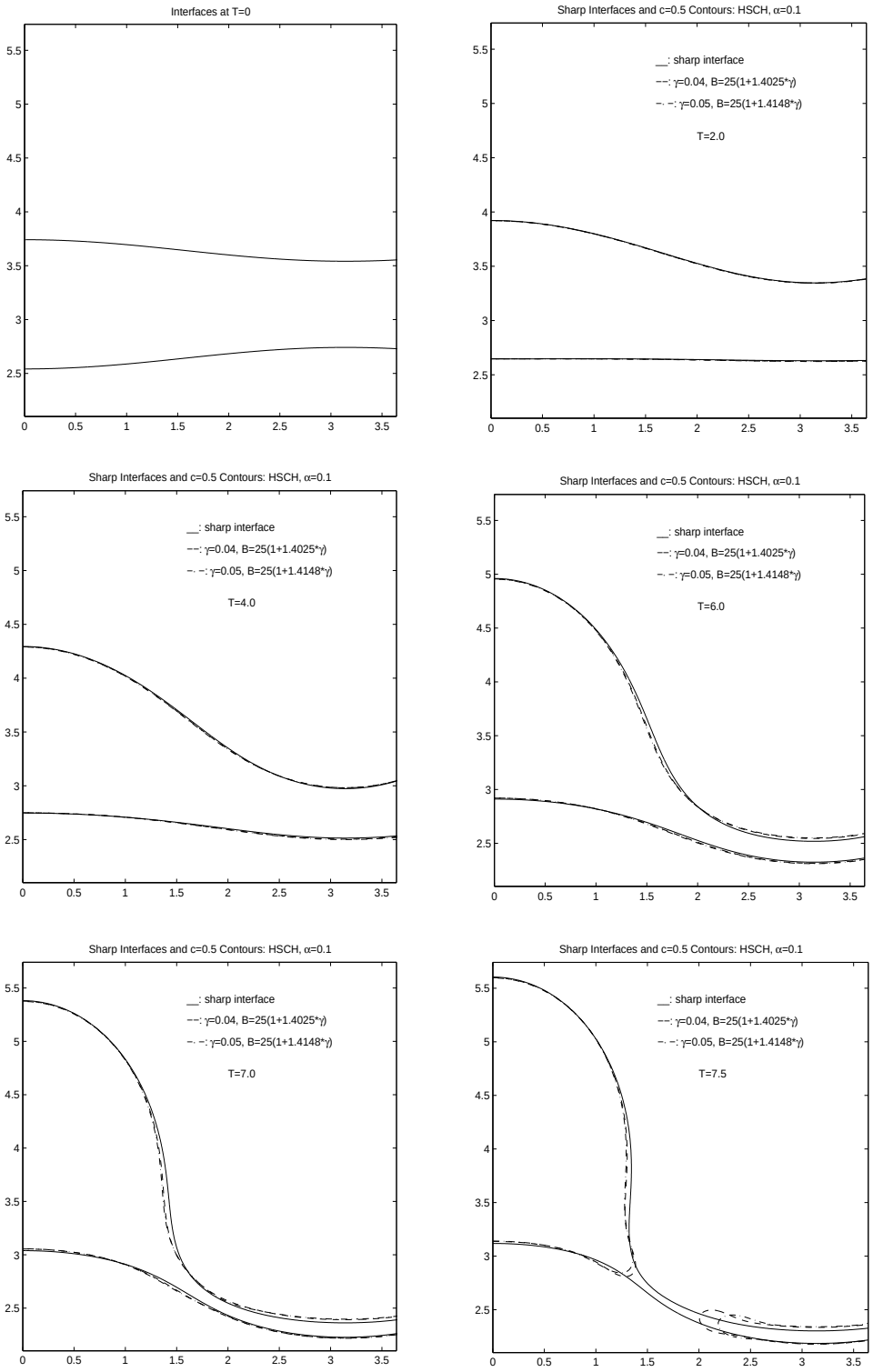

FIG. 19. Lee et al., Phys. Fluids, The effect of modifying the Bond number to match the $k = 1$ sharp interface growth rate. $\alpha = 0.1$ and the $c = 0.5$ contour lines from the HSCH model are shown with $\gamma = 0.04$ (dashed, $|\mathbf{B}| = 25(1 + 1.4025\gamma)$) and $\gamma = 0.05$ (dot-dashed, $|\mathbf{B}| = 25(1 + 1.4148\gamma)$) together with the sharp interface (solid, $|\mathbf{B}| = 25$). Due to symmetry, approximately one half of the layer is shown. (a). $t = 0$; (b). $t = 2.0$; (c). $t = 4.0$; (d). $t = 6.0$; (e). $t = 7.0$; (f). $t = 7.5$.

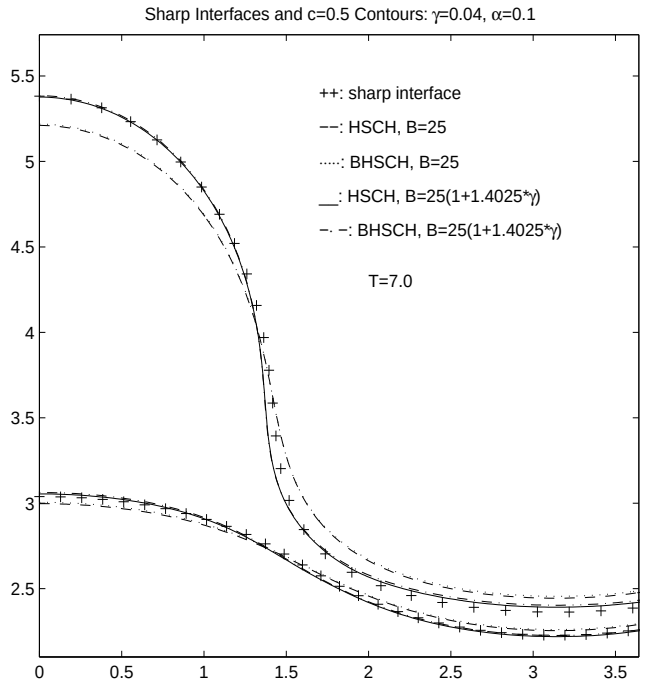

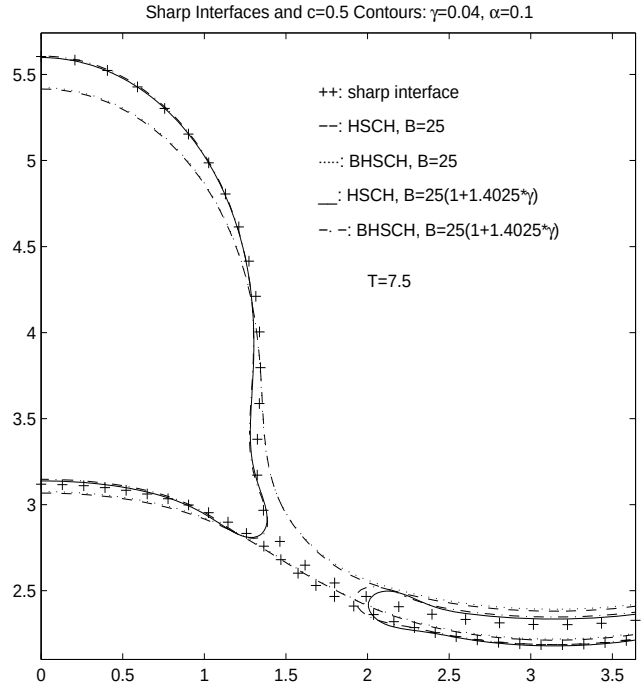

FIG. 20. Lee et al., Phys. Fluids, Close-up of comparison of modified Bond number HSCH $c = 0.5$ contours with the sharp interface result. $\gamma = 0.04$ and $\alpha = 0.1$. Sharp interface (+ curves); HSCH and BHSCH models with $\mathbf{B}| = 25$ (dashed and dotted curves respectively); HSCH and BHSCH models with $|\mathbf{B}| = 25(1 + 1.4025\gamma)$ (solid and dot-dashed curves respectively). (a). $t = 7.0$; (b). $t = 7.5$.

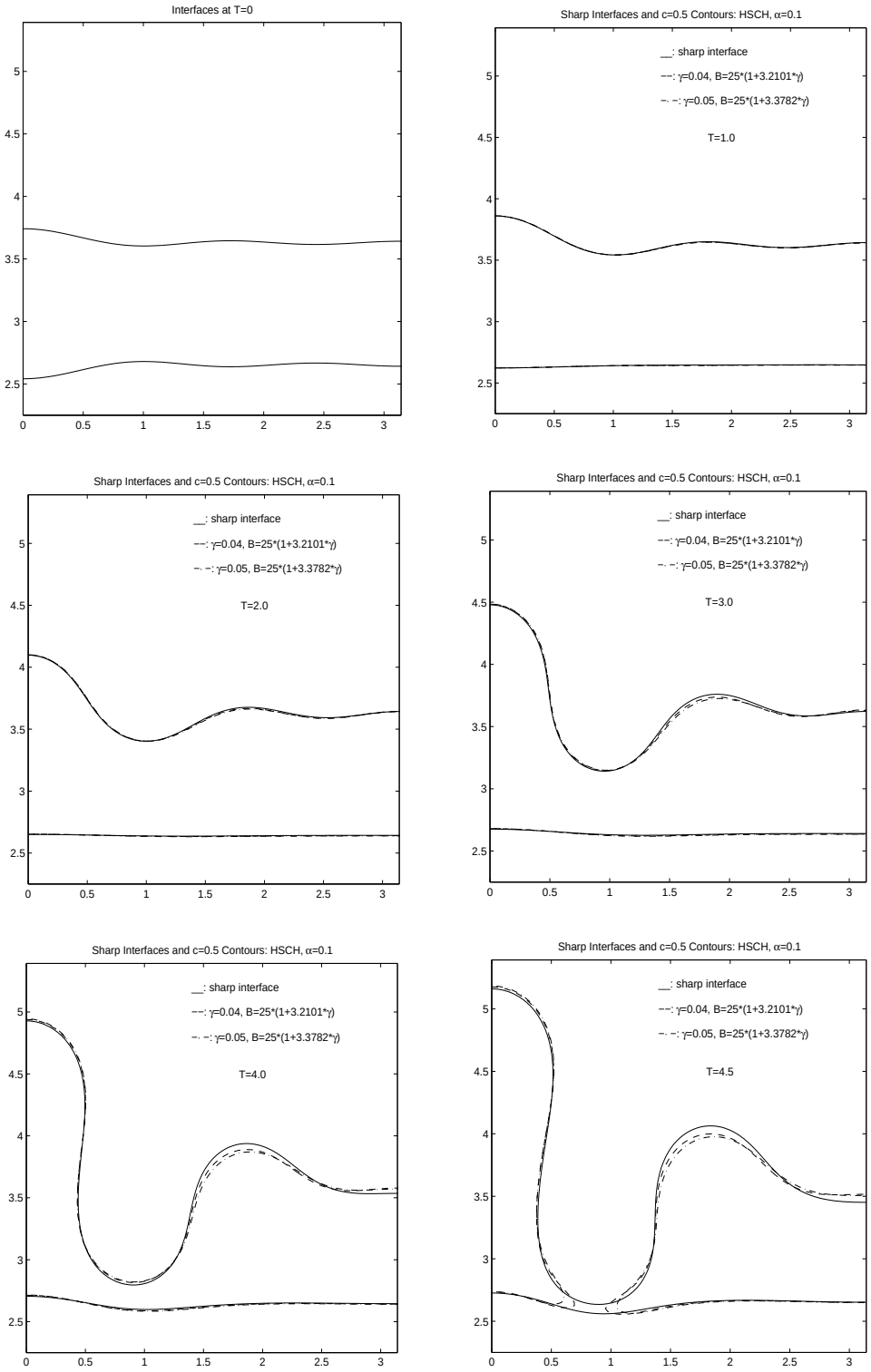

FIG. 21. Lee et al., Phys. Fluids, The effect of modifying the Bond number to match the $k = 3$ sharp interface growth rate. $\alpha = 0.1$ and the $c = 0.5$ contour lines from the HSCH model are shown with $\gamma = 0.04$ (dashed, $|\mathbf{B}| = 25(1 + 3.2101\gamma)$) and $\gamma = 0.05$ (dot-dashed, $|\mathbf{B}| = 25(1 + 3.3782\gamma)$) together with the sharp interface (solid, $|\mathbf{B}| = 25$). Due to symmetry, approximately one half of the layer is shown. (a). $t = 0$; (b). $t = 1.0$; (c). $t = 2.0$; (d). $t = 3.0$; (e). $t = 4.0$; (f). $t = 4.5$.

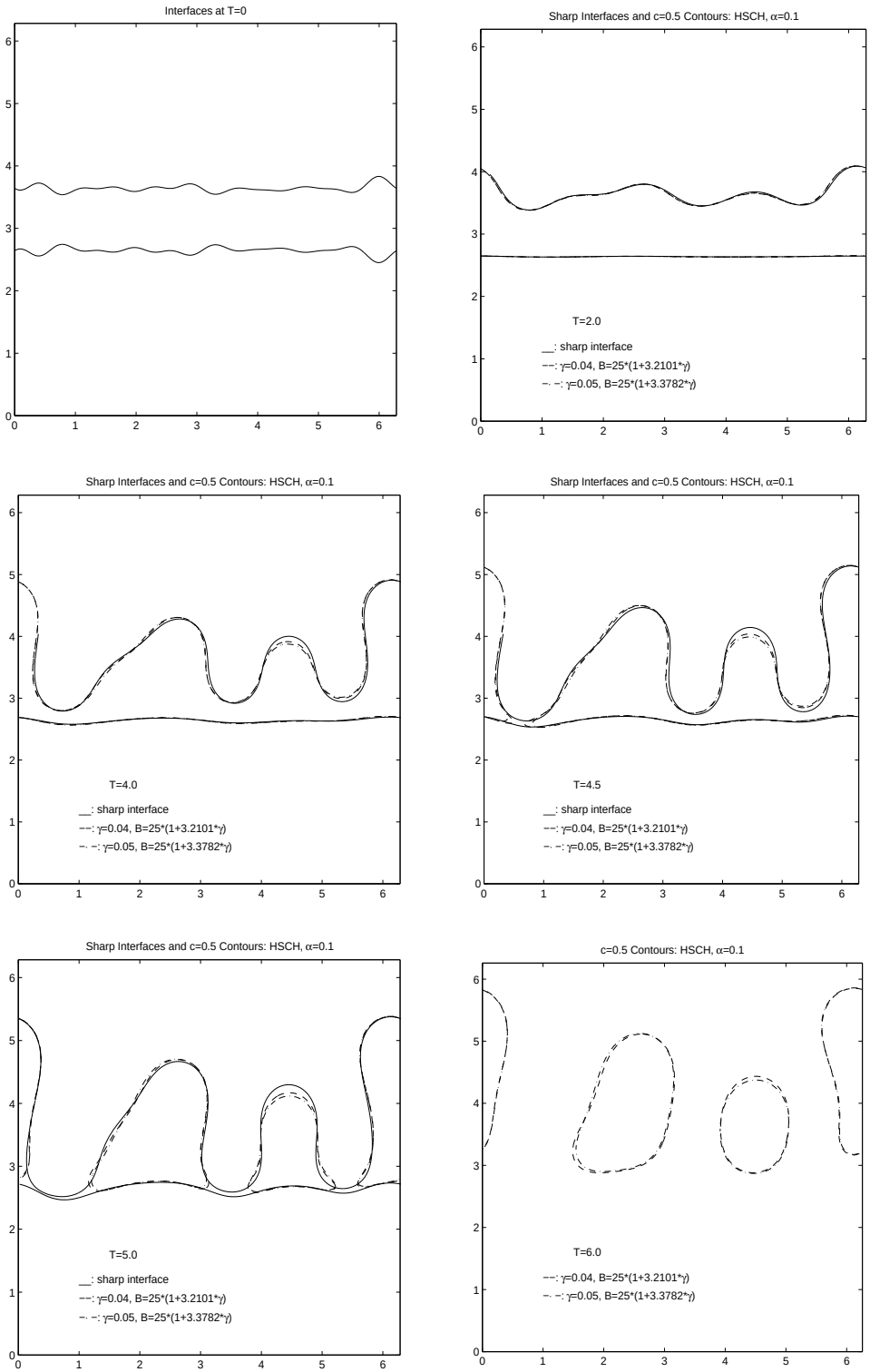

FIG. 22. Lee et al., Phys. Fluids, The effect of modifying the Bond number to match the $k = 3$ sharp interface growth rate with a more complicated, 10 mode initial condition. $\alpha = 0.1$ and the $c = 0.5$ contour lines from the HSCH model are shown with $\gamma = 0.04$ (dashed, $|\mathbf{B}| = 25(1+3.2101\gamma)$) and $\gamma = 0.05$ (dot-dashed, $|\mathbf{B}| = 25(1+3.3782\gamma)$) together with the sharp interface (solid, $|\mathbf{B}| = 25$). (a). $t = 0$; (b). $t = 2.0$; (c). $t = 4.0$; (d). $t = 4.5$; (e). $t = 5.0$; (f). $t = 6.0$.

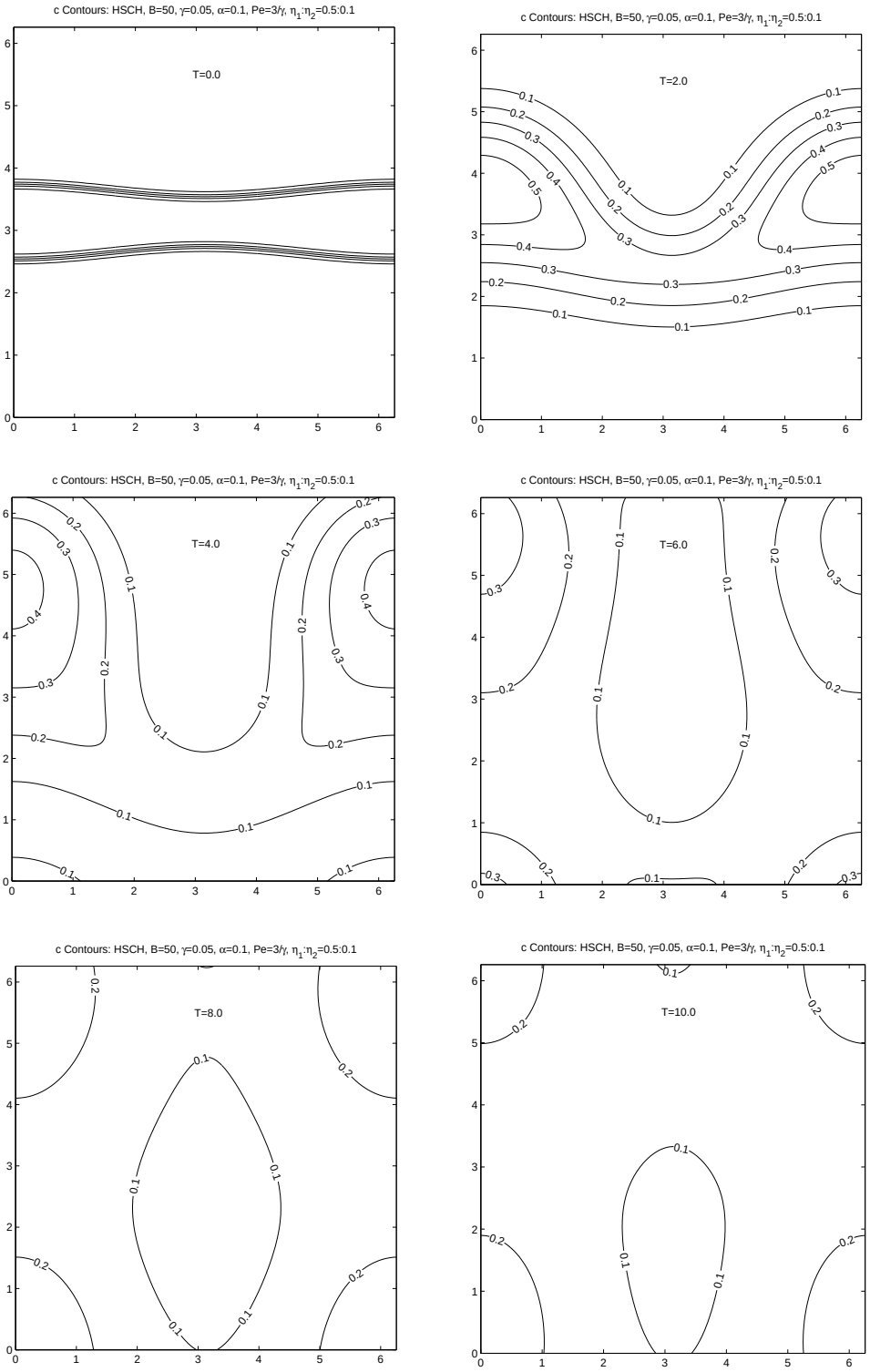

FIG. 23. Lee et al., Phys. Fluids, The effect of miscibility. The contour lines of c are shown from the HSCH model with $|\mathbf{B}| = 50$, $\gamma = 0.05$, $\alpha = 0.1$, $\mathbf{Pe} = 3/\gamma$, $\eta_1 = 0.5$ and $\eta_2 = 0.1$. (a). $t = 0$; (b). $t = 2.0$; (c). $t = 4.0$; (d). $t = 6.0$; (e). $t = 8.0$; (f). $t = 10.0$.

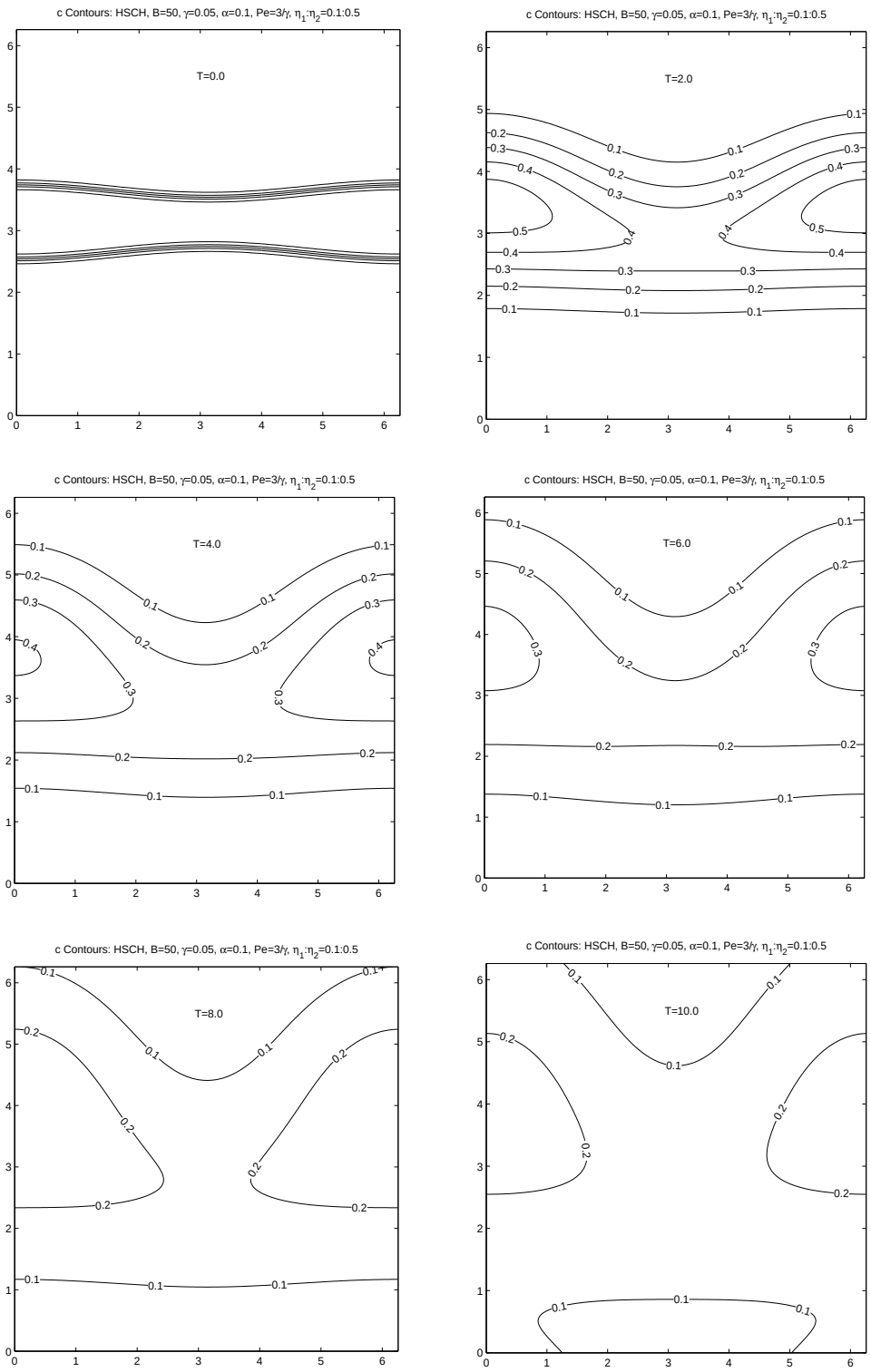

FIG. 24. Lee et al., Phys. Fluids, The effect of miscibility. The contour lines of c are shown from the HSCH model with $|\mathbf{B}| = 50$, $\gamma = 0.05$, $\alpha = 0.1$, $\mathbf{Pe} = 3/\gamma$, $\eta_1 = 0.1$ and $\eta_2 = 0.5$. (a). $t = 0$; (b). $t = 2.0$; (c). $t = 4.0$; (d). $t = 6.0$; (e). $t = 8.0$; (f). $t = 10.0$.

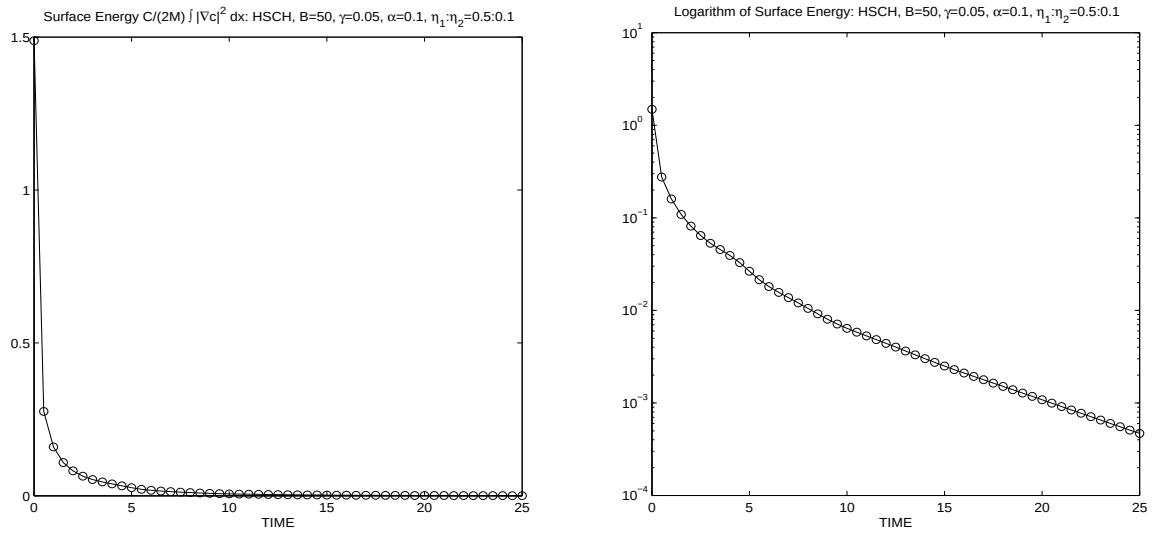

FIG. 25. Lee et al., Phys. Fluids, The evolution of surface energy in the miscible case from figure 23. (a). The surface energy $E_s(t)$; (b). The $\log(E_s(t))$.